Mesoarchean banded iron-formation from the northern Yangtze Craton, South China and its geological and paleoenvironmental implications

Hang Zhou[1], Wenxiao Zhou[1,4*], Yunxu Wei[2,3**], Ernest Chi Fru[4], Bo Huang[5,6], Dong Fu[6], Haiquan Li[1], Mantang Tan[2,3]

[1]*Institute of Geological Survey, China University of Geosciences, Wuhan 430074, China*

[2]*Wuhan Center of China Geological Survey, Wuhan 430205, China*

[3]*Central South China Innovation Center for Geosciences, Wuhan 430205, China*

[4]*School of Earth and Ocean Sciences, Centre for Geobiology and Geochemistry, Cardiff University, Cardiff CF10 3AT, Wales, the United Kingdom*

[5]*National Observation and Research Station for Geohazards, Three Gorges Research Center for Geohazards, China University of Geosciences, Wuhan 430074, China*

[6]*Center for Global Tectonics, State Key Laboratory of Geological Processes and Mineral Resources, China University of Geosciences, Wuhan 430074, China*

* Corresponding author: Wenxiao Zhou (zhouwenxiao@cug.edu.cn)

ORCID: https://orcid.org/0000-0003-4890-8803

** Corresponding author: Yunxu Wei (wyx1856@163.com)

ORCID: https://orcid.org/0000-0003-4429-527X

Abstract

Banded iron formations (BIFs) are important sedimentary rocks used for reconstructing the geochemical and environmental evolution of Precambrian Earth surface conditions. Here, we describe the oldest BIFs of Mesoarchean age in the Yemadong Formation, and their implications for paleo-environmental evolution of the Mesoarchean Ocean in the northern Yangtze Craton, South China. U-Pb dating of metamorphic zircons obtained from metavolcanic rocks interbedded within the Yemadong Complex, record two major tecto-thermal events at 2901 ± 8 Ma, in agreement with a Mesoarchean origin of the Dujiagou BIFs, and as recently as 775 Ma. A high SiO_2+total Fe_2O_3 content of 90.95-94.62 wt.%, moderate 0.54-1.42 wt.% Al_2O_3+TiO_2, and broadly elevated levels of incompatible elements, point to a predominantly chemical origin of the BIF deposit, with a minor but influential terrigenous input. Rare Earth Element (REE) plus Yttrium patterns normalized against Post Archean Average Shale composition are characterized by the depletion of light REE relative to heavy REE. However, extremely weak Eu and Ce anomalies, together with low average chondrite Y/Ho ratios compared to average Mesoarchean BIF values, indicate that the primary REE composition of the BIF may have been diluted to some extent by terrigenous input, pointing to proximity or connection of the depositional setting to a continental margin environment. Despite potential terrigenous dilution of the syngenetic seawater-hydrothermal chemical composition, the preservation of an inherited hydrothermal REE signal in some samples, point to submarine hydrothermal provenance of the Dujiagou BIFs, as is the suggested case for most Precambrian BIFs. Positive $\delta^{56}Fe$ values, ranging from 0.25-0.45 ‰, characteristic of primary Archean BIFs, point to partial oxidation of reduced Fe(II) to divalent (Fe(II)/Fe(III)) magnetite-rich BIFs in a broadly reducing Archean Ocean lacking a persistent and pervasive redoxcline before the rise of atmospheric

44   oxygen.

45   *Keywords*：Banded iron-formation, Iron isotopes, Paleoenvironment, Mesoarchean, Yangtze Craton

46

1. Introduction

48   Banded iron formations (BIFs) are marine chemical sedimentary rocks of predominantly

49   Precambrian origin. They consist mainly of iron-rich layers containing hematite and magnetite

50   alternating with silica-rich bands, composed principally of chert and jasper. Deposition of BIFs in

51   Earth's history is closely related to the secular changes in the atmosphere, hydrosphere, and

52   lithosphere, and thus BIFs are excellent archives for reconstructing the composition and redox state

53   of the ancient ocean-atmosphere system under which they formed (Bolhar et al., 2004; Klein, 2005;

54   Polat and Frei, 2005; Bekker et al., 2010; Basta et al., 2011; Mloszewska et al., 2012; Zhang et al.,

55   2012; Cui et al., 2014; Brando Soares et al., 2017; Ghosh and Baidya, 2017; Huang et al., 2019).

56   Three principal types of BIFs are known, defined primarily by their depositional environment

57   (Bekker et al., 2010; Li et al., 2014a; Hagemann et al., 2016). Algoma-type BIFs deposited in deep-

58   sea island arc environments, and near subduction trenches. They are generally the most common

59   BIFs found in Archean greenstone belts associated with old cratonic sequences (Goodwin, 1973;

60   Klein, 2005)—are small in scale, with the oldest known deposit formed ~3.8 billion years ago (Ga)

61   in the Isua greenstone belt, West Greenland (Myers, 2001; Bolhar et al., 2004; Polat and Frei, 2005;

62   Czaja et al., 2013). Superior-type BIFs are larger in scale, compared to Algoma-type BIFs. They

63   formed mainly in oxidized environments lacking syn-depositional volcanic assemblages, and are

64   found deposited with transgressive successions that formed on shallow continental shelves located

65   in intra-cratonic Basins (Klein, 2005; Li et al., 2012a; Li et al., 2014a). The Neoarchean and early

66   Paleoproterozoic intervals witnessed prolific Superior-type BIF deposition, with examples found in

67   the Hamersley Basin of Western Australia and the Transvaal Supergroup, South Africa (Morris,

68   1993; Johnson et al., 2003; Bekker et al., 2010; Smith, 2018). Large-scale BIF deposition terminated

69   at ~1.8 Ga, when they disappeared from the marine sedimentary rock record, before an abrupt but

70   brief reappearance of Rapitan-type BIFs in conjunction with the Neoproterozoic snowball Earth

71   glaciations, ~0.7-0.635 Ga (Hoffman et al., 1998). The long depositional history of BIFs, timing and

72   coincidence with major redox, climatic and geochemical changes in the ocean-atmosphere system,

73   has led to their wide use as reliable proxies for Earth oxygenation history and the evolution of the

74   Precambrian crust (Crowley et al., 2002; Holland, 2006; Jenner et al., 2009; Poulton and Canfield,

75   2011; Kasting, 2013; Chi Fru et al., 2016; Chi Fru et al., 2018).

76   Although the timing and extent of Earth surface oxidation before the Paleoproterozoic Great

77   Oxidation Event (GOE), ~2.4 -2.0 Ga remains debated (Czaja et al., 2013), most workers agree that

78   atmospheric O_2 contents were low in the Archean (e.g., Farquhar et al. (2000); Anbar et al. (2007);

79   Guo et al. (2009)). In line with this observation, the chemical composition of Archean BIFs often

80   contain both reduced and oxidized iron reservoirs, with the deposition of BIFs 3.8–1.8 Ga taken as

81   compelling evidence for the prevalence of anoxic iron rich waters that enabled high iron mobility

82   in the marine realm (Poulton and Canfield, 2011). The Early Paleoproterozoic GOE and the Late

83   Neoproterozoic Oxidation Event, NOE (e.g., Och and Shields-Zhou (2012); Lyons et al. (2014)),

84   are proposed as the principal reason for the eventual disappearance of BIFs from the marine

85   sedimentary rock record (Poulton and Canfield, 2011).

86   Because of their great antiquity, in many instances, the primary chemical composition of BIFs

87   has been altered by post-depositional diagenetic and metamorphic processes. Nonetheless, a

88 substantial body of work suggests that Fe isotopes are particularly resistant to these secondary post-

89 depositional changes in bulk BIF composition (Dauphas and Rouxel, 2006; Frost et al., 2006;

90 Dauphas et al., 2007a; Czaja et al., 2013). Consequently, iron isotopes often play an important role

91 in the study of BIFs, and their distribution in BIFs used frequently to track global early Earth surface

92 redox evolution and the workings of the early biogeochemical elemental cycles (Johnson et al., 2003;

93 Dauphas et al., 2004; Dauphas et al., 2007a; Dauphas et al., 2007b; Hyslop et al., 2008; Johnson et

94 al., 2008; Li et al., 2012b; Chi Fru et al., 2013; Czaja et al., 2013; Wang et al., 2017).

95   In China, most Neoarchean-Paleoproterozoic BIFs are deposited in the North China Craton (Li

96 et al., 2012b; Wang et al., 2014; Wang et al., 2017; Wu et al., 2020), while the presence of BIFs in

97 the older Mesoarchean South China Block, host to the Yangtze Craton, remains poorly explored.

98 Consequently, there exists a considerable gap in our understanding of the redox and biogeochemical

99 development of the iron-rich Mesoarchean oceans in the Yangtze Craton. This has major

100 implications for the global evolution of the early ocean-atmosphere system, with respect to the

101 independent development of the South China Mesoarchean Block. In this paper, we coupled new

102 U–Pb LA-ICP-MS ages to elemental and iron isotope geochemistry, to constrain the depositional

103 age and genesis of Dujiagou BIFs in the Mesoarchean Yangtze Craton of the South China Block,

104 and the contemporaneous marine conditions in which they formed.

105

106 **2. Regional geology**

107   The South China Block is one of the largest cratonic blocks in East Asia and is generally

108 divided into the Yangtze Craton in the northwest and the Cathaysia Block in the southeast, separated

109 by the intervening Jiangnan orogenic belt ((Li et al., 2003; Zhao and Guo, 2012; Zhao and Cawood,

110　2012; Charvet, 2013; Zhai, 2013; Cawood et al., 2018);**Figure 1a**). Located to west of the Qinghai

111　Tibet Plateau and south of the Qinling Dabie Sulu orogenic belt, the Yangtze Craton is composed

112　mainly of late Paleoproterozoic and Neoproterozoic rocks with sporadic outcrops of Archean rocks

113　(Zhao and Cawood, 2012; Zhang and Zheng, 2013; Ji et al., 2014; Jiang et al., 2016; Han et al.,

114　2017; Wei et al., 2020). The Huangling dome, located in the northern part of the Yangtze Craton, is

115　the only area where both Archean and Paleoproterozoic metamorphic rocks are exposed in the

116　region (Gao et al., 1999; Qiu et al., 2000; Zheng et al., 2006; Gao et al., 2011; Chen et al., 2013;

117　Han et al., 2018). They provide a natural laboratory for studying the extensive tecto-magmatic and

118　metamorphic processes that occurred during the tectonic evolution of the Yangtze Craton.

119　　　　The Kongling terrane, a major Archean relic exposed in the center of the Huangling dome，

120　covers an area of ~ 360 km^2 (Peng et al., 2009; Wei et al., 2019). These Archean rocks were intruded

121　by the late Paleoproterozoic ~1.85 Ga Quanqitang A-type granites and the Neoproterozoic ~0.85

122　Ga Huangling granitoids in the north and south, respectively. The rocks are unconformably overlain

123　by a Neoproterozoic and Paleozoic sedimentary sequence that has experienced negligible

124　metamorphic alteration (Li et al., 2003; Peng et al., 2009; Peng et al., 2012a; Peng et al., 2012b;

125　Zhao et al., 2013; Han et al., 2018). Regionally, the Wuduhe Fault divides the the Kongling terrane

126　into the North and South Konling Terranes, abbreviated as NKT and SKT, respectively (**Figure 1**b).

127　The NKT is considered metamorphosed to amphibolite facies (Jiang, 1986; Ling et al., 2001; Wei

128　and Jing, 2013; Wei et al., 2020) and to be compose mainly of the Mesoarchean 2.9-3.0 Ga

129　Dongchonghe tonalitic-trondhjemitic-granodioritic (TTG) gneiss, granitic gneiss, and locally

130　preserved amphibolites. The protolith of most of the amphibolites is considered to be 3.2-3.0 Ga

131　ultramafic-mafic rocks—the oldest known lithologies in the Huangling basement, the maintain

132   constituent of the Huangling greenstone belt, HGB (Xiong et al., 2004; Wei et al., 2019; Wei et al.,

133   2020; Wei, 2021). Based on chronological and petrological evidence, the Yemadong Complex is

134   considered a relic of the HGB, named for its location near the Yemadong village (**Figure 1**c) (Wei

135   et al., 2019; Zhou et al., 2019; Wei et al., 2020; Wei, 2021). Therefore, the lithological association

136   of the Yemadong Complex inherits the HGB (Zhou et al., 2019). Their original igneous texture is

137   almost obscured and their primary mineral composition replaced by secondary metamorphic

138   minerals (Wei, 2021).
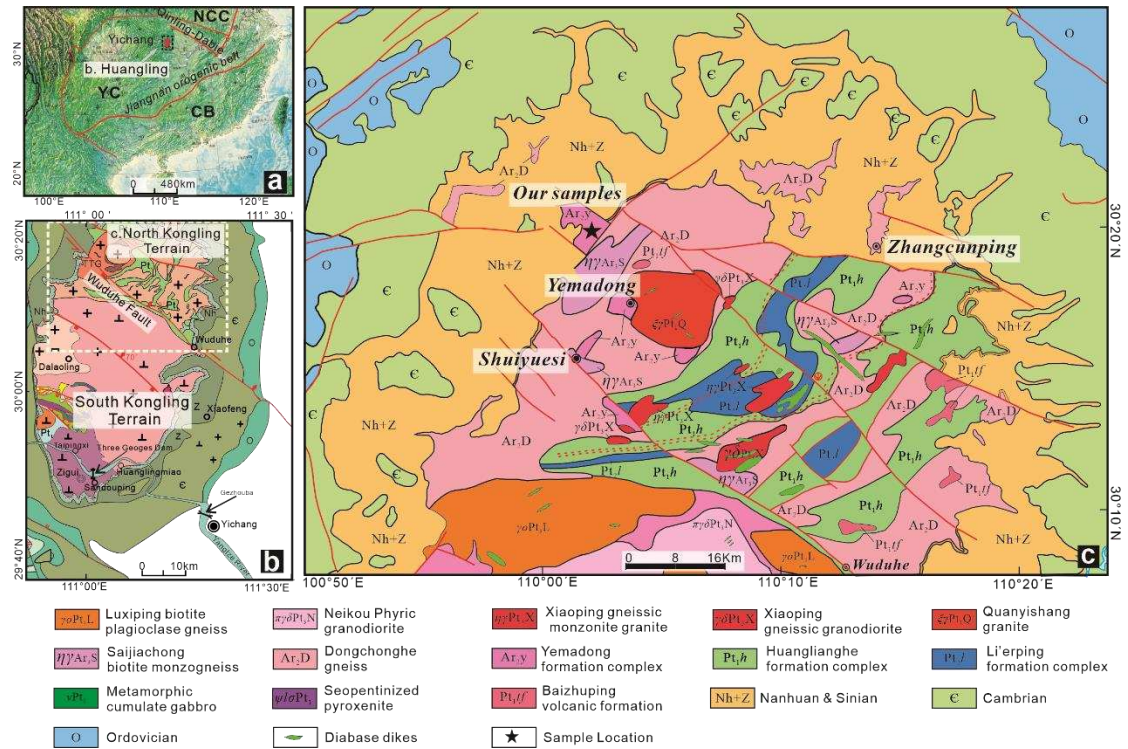
140   **Figure 1.** (a) Simplified tectonic map of major Precambrian blocks in South China, (b) Detailed tectonic map of the
141   Kongling area on the northern margin of the Yangtze Craton, (c) Geological map showing the Huangling dome in
142   Yichang City as well as the sampling locations, modified after Wei et al. (2019).

144   In the Huangling dome, the Yemadong Complex is divided into three portions based on

145   lithology and structural position, the lowest part composed of biotite-tremolite and magnetite-

146   bearing plagioclase-amphibole schist, considered to have originated from an ultrabasic-basic

147   volcanic rock protolith. The middle portion is composed of biotite-plagioclase gneiss, feldspathic

7

148   quartzite, and the banded magnetite quartzite discussed in this paper. The upper section is comprised

149   mainly of leptynite, leptite metamorphic intermediate and acidic volcanic rocks (Zhou et al., 2019).

150   The Dujiagou BIFs occur in the middle and upper part of the greenstone sequence of Yemadong

151   Complex (HGB residue), consistent with the occurrence of most Precambrian BIFs in the greenstone

152   belt sequence (e.g., Ghosh and Baidya (2017) and Singh and Slabunov (2015)).

153   In the field, they are exposed as four stratified BIF layers that are generally 20-50 cm thick,

154   dominated by magnetite and quartzite with characteristic quartz and magnetite enrichment (**Figure**

155   **2a-c**). The magnetite and quartzite layers present a black and white stripe appearance, characterized

156   by interbedded light-colored quartz and dark-colored magnetite stripes (**Figure 2d, e**). Magnetite is

157   generally Subhedral or heteromorphic, with a grain size of 0.1-0.2 mm and a Fe content of 45-50%.

158   In the magnetite-rich stripes, the grains are larger and interconnected, forming aggregates and

159   irregular bedding planes, while magnetite is sparsely disseminated among quartz grains in the

160   magnetite-poor stripes to form small, separate grains. Overall, the mineral assemblage in the sample

161   is simple, consisting predominantly of quartz and magnetite with lesser amounts of actinolite and

162   other accessory minerals (**Figure 2f, g**).

163
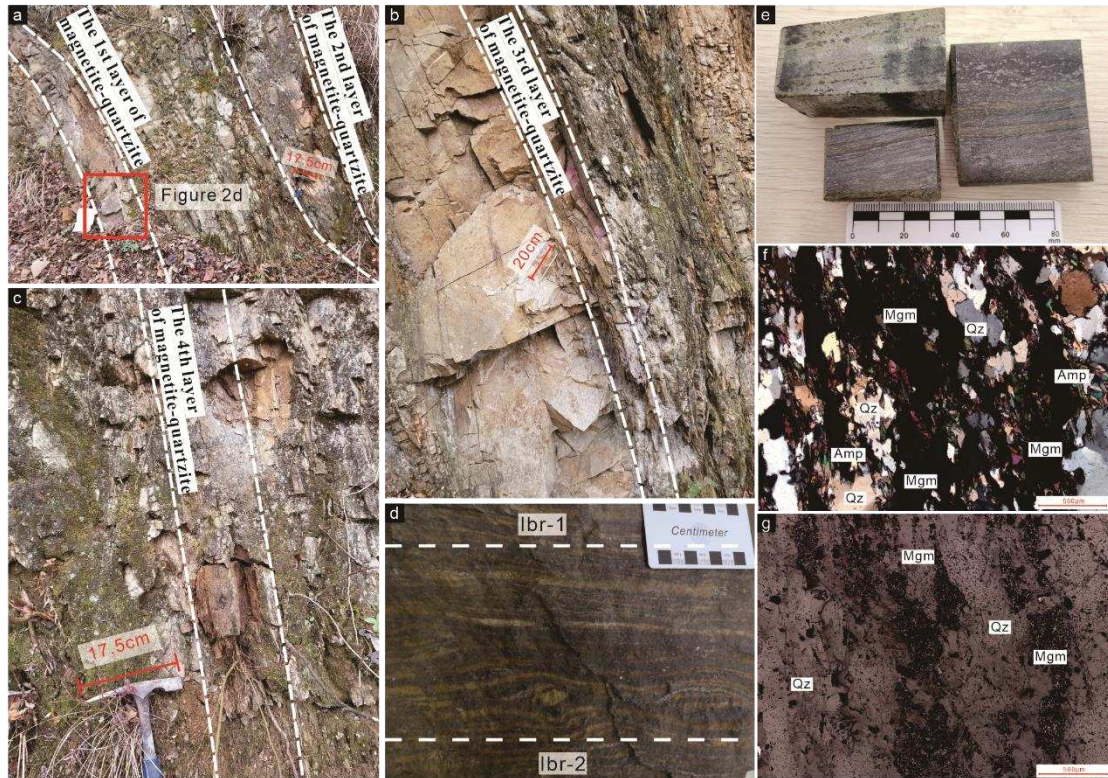
Figure 2. Representative photographs of the Dujiagou BIF. (a-c) Field photographs showing the outcrop of Dujiagou

Algoma-type BIFs interbedded with felsic metavolcanic rocks, (d) Banded magnetite and quartzite layers composed

of bands of dark color magnetite alternating with white color quartz layers. The Ibr-1 and Ibr-2 layers were sampled

for iron isotope analysis, (e) An example of a fresh surface cut from the magnetite and quartzite layers in Figure 2d,

(f-g) BIF mainly consisting of alternating magnetite Fe-oxide and quartz bands with other minor minerals (e-

Polarized Light; f- Reflected Light), Qz stands for quartz, Mgm for magnetite and Amp for amphibole.

3. Analytical methods

In order to ensure the validity of the data and exclude the influence of weathering conditions

on the analysis, exposed weathered surfaces of 13 representative magnetite and quartzite sample

were cut and only the fresh portion (**Figure 2e**) used for the determination of major, trace and rare

earth element contents.

3.1. Zircon U-Pb dating

U-Pb dating and trace element analysis of zircon were simultaneously conducted by LA-ICP-MS at Wuhan Sample Solution Analytical Technology Co., Ltd., Wuhan, China. Detailed operating conditions for the laser ablation system and the ICP-MS instrument and data reduction are the same as described by Zong et al. (2017). Laser sampling was performed using a GeolasPro laser ablation system consisting of a COMPexPro 102 ArF excimer laser with a wavelength of 193 nm, a maximum energy of 200 ml, and a MicroLas optical system. A "wire" signal smoothing device was included with the laser ablation system (Hu et al., 2015). An Agilent 7700e ICP-MS instrument was used to acquire ion-signal intensities. The sample was deliver using the make-up gas argon, mixed with the carrier gas helium via a T-connector before entry into the ICP. The spot size and laser frequency were set to 32 µm and 5 Hz, respectively. Zircon 91500 and glass NIST610 were used as external standards for U-Pb dating and trace element calibration, respectively. Each analysis incorporated a background acquisition of approximately 20-30 s followed by 50 s of sample data acquisition. An Excel-based software ICPMSDataCal was used to perform off-line selection and integration of background and analyzed signals, time-drift correction and quantitative calibration for trace element analysis and U-Pb dating. Concordia diagrams and weighted mean calculations were made using Isoplot/Ex_ver4.15.

3.2. Bulk-rock major element

Bulk-rock major element analysis was conducted with an XRF Primus Ⅱ, Rigaku (Japan) instrument at Wuhan Sample Solution Analytical Technology Co., Ltd., Wuhan, China. The detailed sample-digestion procedure was as follows: (1) Sample powder (200 mesh) were placed in an oven set at 105℃ and dried for 12 hours; (2) ~1.0 g dried sample was accurately weighted and placed in

199 ceramic crucibles and heated in a muffle furnace at 1000°C for 2 hours. After cooling to 400°C,

200 samples were placed in a drying vessel and weighed again in order to calculate the loss on ignition

201 (LOI); (3) 0.6 g sample powder was mixed with 6.0 g $Li_2B_4O_7$: $LiBO_2$: LiF = 9:2:1 cosolvent and

202 0.3 g NH_4NO_3 oxidant in a Pt crucible and heated in a furnace for 1150°C at 14 min. The melted

203 samples were quenched with air for 1 min to produce flat discs on the fire brick for XRF analyses.

204 **3.3. Bulk-rock trace element**

205 Bulk-rock trace element analysis was conducted on an Agilent 7700e ICP-MS at Wuhan

206 Sample Solution Analytical Technology Co., Ltd., Wuhan, China. Sample powders were prepared

207 and dried in an oven at 105°C as described in section 3.2, after which 50 mg of the dried powder

208 was accurately weighed and placed in Teflon bombs. This was followed by the slow addition of 1

209 ml HNO_3 and 1 ml HF. The Teflon bombs were then put in a stainless steel pressure jacket and

210 heated to 190 °C in an oven for >24 hours. After cooling, the Teflon bombs were opened and placed

211 on a hotplate at set at 140°C and evaporated, followed by the addition of 1 ml HNO_3 and another

212 round of evaporation to dryness. To the dried sample was added 1 ml HNO_3, 1ml MQ water and 1

213 ml 1 ppm internal standard solution. The Teflon bombs were resealed and placed in the oven at 190°C

214 for >12 hours. The final solution was transferred to a polyethylene bottle and diluted to 100 g with

215 2% HNO_3.

216 **3.4. Bulk-rock Fe isotope**

217 Iron isotopic measurements were performed on a Nu Plasma 1700 MC-ICP-MS (Nu

218 Instruments, Wrexham, UK) at the State Key Laboratory of Geological Processes and Mineral

219 Resources, China University of Geosciences, Wuhan. Typically, ~1.0 g sample powders were

220 weighed into individual Teflon beakers and dissolved in a mixture of HF-HNO_3-HCl-$HClO_4$. Iron

221   was purified using the AG1X-8 (200–400 mesh chloride form, Bio-Rad, Hercules, CA, USA) resin

222   in HCl media. Matrix elements were removed by 8 ml 6 mol/L HCl, and Fe was then collected by

223   9 ml 0.4 mol/L HCl. The same column procedure was repeated twice to ensure complete elimination

224   of the matrices. The final Fe eluate was acidified with 100 μl of concentrated HNO_3. The dried

225   sample was then dissolved in 3% HNO_3 for isotopic determination. Double distilled acids and

226   Optima^{TM} ultra pure $HClO_4$ were used. The whole procedure Fe blank was < 0.01% of the processed

227   samples and therefore considered negligible. Samples were introduced into the Ar plasma using a

228   Cetac ASX-100 auto sampler through a Thermo Scientific Stable Introduction System (SIS), which

229   consists of quartz cyclonic and Scott-type spray chambers and a set of PFA Teflon self-aspirating

230   micro-nebulisers with different uptake rates (45, 50, 100 μl min^{-1}). The instrument mass bias was

231   routinely corrected by calibrator sample bracketing. Data were processed offline and reported in the

232   δ notation (δ ^{x}Fe (‰) = [(^{x}Fe/^{54}Fe)$_{sample}$ / (^{x}Fe/^{54}Fe)$_{calibrator}$ - 1]*1000, where x is 56 or 57 and

233   (^{x}Fe/^{54}Fe) calibratoris the average of the two bracketing calibrators). Most tests carried out in this

234   study used GSB Fe (an ultrapure single elemental standard solution from the China Iron and Steel

235   Research Institute) as an in-house reference solution (He et al., 2015).

Table 1. U-Pb age data of zircons from the metamorphic mafic rocks interbedded in Dujiagou BIFs

Testing No.	Concentrations (ppm)				Isotopic ratios								$^{207}Pb/^{206}Pb$		$^{207}Pb/^{235}U$		$^{206}Pb/^{238}U$		$^{208}Pb/^{232}Th$		Comments
	Pb	Th	U	Th/U	$^{207}Pb/^{206}Pb$	1σ	$^{207}Pb/^{235}U$	1σ	$^{206}Pb/^{238}U$	1σ	$^{208}Pb/^{232}Th$	1σ	Age (Ma)	1σ	Age (Ma)	1σ	Age (Ma)	1σ	Age (Ma)	1σ	
D5216-01	1825	64.1	484	0.13	0.2072	0.0035	16.0880	0.2833	0.5637	0.0131	0.1380	0.0041	2884	18	2882	17	2882	54	2613	72	Concordant
D5216-02	2167	140	782	0.18	0.2078	0.0029	16.3513	0.2948	0.5681	0.0116	0.1465	0.0041	2888	15	2898	17	2900	48	2763	73	Concordant
D5216-03	2068	105	790	0.13	0.1871	0.0029	10.5673	0.2509	0.4092	0.0110	0.1154	0.0039	2717	20	2486	22	2211	50	2207	71	Disconcordant
D5216-04	374	82.6	714	0.12	0.1865	0.0032	9.8135	0.3361	0.3781	0.0116	0.1032	0.0035	2712	25	2417	32	2067	54	1985	63	Disconcordant
D5216-05	192	166	1609	0.1	0.1075	0.0030	1.5302	0.0317	0.1033	0.0019	0.0299	0.0006	1757	52	943	13	634	11	596	11	Positive Eu
D5216-06	633	117	993	0.12	0.1972	0.0035	13.1472	0.4356	0.4784	0.0138	0.1295	0.0054	2803	24	2690	31	2520	60	2460	97	Disconcordant
D5216-07	900	73.4	580	0.13	0.2084	0.0039	16.3973	0.3808	0.5698	0.0133	0.1521	0.0059	2893	17	2900	22	2907	55	2861	104	Concordance
D5216-08	638	83.7	798	0.1	0.2081	0.0033	16.0604	0.3027	0.5575	0.0108	0.1558	0.0051	2891	14	2880	18	2856	45	2927	89	Concordance
D5216-09	639	89.6	754	0.12	0.2101	0.0034	16.3341	0.3041	0.5629	0.0117	0.1666	0.0051	2906	15	2897	18	2878	48	3114	88	Concordance
D5216-10	675	90.4	751	0.12	0.2082	0.0028	16.0273	0.2622	0.5556	0.0108	0.1617	0.0044	2891	14	2878	16	2848	45	3029	76	Concordance
D5216-11	531	75.3	634	0.12	0.2099	0.0032	16.3240	0.2665	0.5627	0.0119	0.1604	0.0046	2905	16	2896	16	2878	49	3007	80	Concordance
D5216-12	2162	81	539	0.15	0.2096	0.0033	16.4806	0.2857	0.5686	0.0132	0.1666	0.0047	2903	18	2905	17	2902	54	3115	82	Concordance
D5216-13	984	63.1	529	0.12	0.2117	0.0033	16.7031	0.3893	0.5701	0.0159	0.1666	0.0051	2919	20	2918	22	2908	65	3114	88	Concordance
D5216-14	2173	130	1096	0.12	0.1485	0.0055	3.7124	0.1000	0.1814	0.0046	0.0509	0.0013	2328	65	1574	22	1074	25	1003	25	Positive Eu
D5216-15	505	85.5	732	0.12	0.2001	0.0032	13.3950	0.2264	0.4855	0.0116	0.1320	0.0038	2827	19	2708	16	2551	50	2506	67	Disconcordant
D5216-16	323	60.7	1068	0.06	0.1611	0.0053	6.3583	0.1352	0.2863	0.0071	0.0797	0.0020	2467	57	2027	19	1623	36	1550	38	Positive Eu
D5216-17	474	138	1094	0.13	0.1708	0.0026	7.4467	0.1464	0.3154	0.0078	0.0913	0.0025	2566	19	2167	18	1767	38	1765	45	Disconcordant
D5216-18	1981	195	1660	0.12	0.1218	0.0070	1.3469	0.0627	0.0802	0.0027	0.0230	0.0008	1983	105	866	27	497	16	459	15	Positive Eu
D5216-19	1355	53.4	429	0.12	0.2065	0.0031	16.1155	0.3200	0.5642	0.0141	0.1460	0.0043	2879	19	2884	19	2884	58	2755	77	Concordance
D5216-20	1152	69.8	629	0.11	0.2107	0.0034	16.3426	0.2878	0.5617	0.0132	0.1524	0.0047	2911	18	2897	17	2874	54	2866	82	Concordance
D5216-21	453	92.8	739	0.13	0.1931	0.0037	11.4320	0.3174	0.4276	0.0123	0.1185	0.0035	2768	21	2559	26	2295	55	2264	63	Disconcordant
D5216-22	460	165	1309	0.13	0.1778	0.0029	6.7369	0.3240	0.2717	0.0130	0.0797	0.0042	2632	36	2077	43	1549	66	1549	79	High U
D5216-23	2614.9	41.9	1297	0.03	0.1104	0.0047	1.4999	0.0479	0.0985	0.0028	0.0285	0.0009	1806	80	930	19	606	16	568	18	Positive Eu
D5216-24	2147	125	830	0.15	0.1843	0.0033	8.4064	0.2898	0.3281	0.0119	0.0926	0.0044	2692	27	2276	31	1829	58	1789	81	Disconcordant
D5216-25	2301	73.2	570	0.13	0.1977	0.0032	12.9525	0.2619	0.4732	0.0123	0.1335	0.0048	2807	20	2676	19	2498	54	2533	85	Disconcordant
D5216-26	922	196	1283	0.15	0.1661	0.0039	7.2453	0.1569	0.3034	0.0076	0.0907	0.0031	2518	19	2142	19	1708	37	1755	58	Positive Eu
D5216-27	1673	67.2	539	0.12	0.2096	0.0069	14.9327	0.3300	0.5167	0.0127	0.1403	0.0035	2902	55	2811	21	2685	54	2654	63	Disconcordant
D5216-28	1765	92	781	0.12	0.1776	0.0032	8.2399	0.3728	0.3299	0.0135	0.0979	0.0043	2630	34	2258	41	1838	66	1888	80	Disconcordant
D5216-29	1977	38.1	323	0.12	0.2079	0.0039	16.4853	0.3260	0.5732	0.0152	0.1687	0.0054	2889	20	2905	19	2921	62	3151	94	Concordance
D5216-30	3160	163	1253	0.13	0.1045	0.0052	1.3829	0.0548	0.0960	0.0029	0.0279	0.0008	1705	94	882	23	591	17	556	17	Positive Eu
D5216-31	467	72.3	528	0.14	0.2101	0.0036	16.3015	0.3614	0.5588	0.0152	0.1649	0.0048	2907	20	2895	21	2862	63	3086	83	Concordance
D5216-32	2653	50.1	444	0.11	0.2079	0.0037	16.2793	0.3365	0.5689	0.0172	0.1623	0.0046	2889	24	2893	20	2903	71	3040	79	Concordance
D5216-33	298	313	1546	0.2	0.1256	0.0039	2.1096	0.0972	0.1151	0.0044	0.0359	0.0016	2037	37	1152	32	702	25	714	32	High U

Testing No.	Concentrations (ppm)				Isotopic ratios								207Pb/206Pb		207Pb/235U		206Pb/238U		208Pb/232Th		Comments
	Pb	Th	U	Th/U	207Pb/206Pb	1σ	207Pb/235U	1σ	206Pb/238U	1σ	208Pb/232Th	1σ	Age (Ma)	1σ	Age (Ma)	1σ	Age (Ma)	1σ	Age (Ma)	1σ	
D5216-34	1125	346	2521	0.14	0.0796	0.0046	0.6444	0.0296	0.0587	0.0021	0.0176	0.0006	1188	118	505	18	368	13	352	12	Positive Eu
D5216-35	2004	219	1649	0.13	0.1155	0.0055	1.3622	0.0500	0.0855	0.0026	0.0246	0.0007	1888	88	873	21	529	15	491	15	Positive Eu
D5216-36	1191	875	1362	0.64	0.1905	0.0034	6.6736	0.3390	0.2492	0.0115	0.0458	0.0024	2746	37	2069	45	1434	59	905	47	Positive Eu
D5216-37	693	70.9	673	0.11	0.2142	0.0032	16.7282	0.2881	0.5650	0.0121	0.1579	0.0051	2937	16	2919	17	2887	50	2964	90	Concordance
D5216-38	275	149	1816	0.08	0.1059	0.0039	1.3545	0.0355	0.0928	0.0024	0.0269	0.0007	1730	70	870	15	572	14	537	14	High U
D5216-39	734	93.8	764	0.12	0.2112	0.0037	14.3764	0.3260	0.4926	0.0128	0.1423	0.0053	2915	19	2775	22	2582	55	2689	94	Disconcordant
D5216-40	318	202	1704	0.12	0.1309	0.0135	1.9136	0.1589	0.1060	0.0065	0.0301	0.0018	2110	188	1086	55	650	38	600	36	High U
D5216-41	618	92.5	991	0.09	0.1835	0.0036	9.9423	0.2736	0.3916	0.0116	0.1125	0.0051	2685	22	2429	25	2130	54	2154	92	Concordance
D5216-42	436	65.4	634	0.1	0.1972	0.0052	10.5984	0.2424	0.3819	0.0103	0.1117	0.0051	2803	20	2489	21	2085	48	2139	93	Concordance
D5216-43	462	44.1	495	0.09	0.2110	0.0038	16.4915	0.3976	0.5712	0.0182	0.1614	0.0056	2913	24	2906	23	2913	75	3025	97	Concordance
D5216-44	789	95.1	700	0.14	0.2112	0.0030	16.7125	0.2901	0.5717	0.0123	0.1533	0.0046	2915	16	2918	17	2915	51	2883	80	Concordance
D5216-45	701	106	1042	0.1	0.1896	0.0050	11.0389	0.3262	0.4051	0.0133	0.1151	0.0043	2739	24	2526	28	2193	61	2201	78	Concordance

37 The obtained concordia age (1063.6 ± 3.6 Ma, n = 20) and 207Pb/235U age (1063.5 ± 7.3 Ma, n = 20) of zircon standard 91500 agrees well with the preferred ID-TIMS 207Pb/235U age of 1065.4 ± 0.3

38 Ma (Jackson et al., 2004) within analytical uncertainty.

239   **Table 2**. major element (wt. %) and trace element (ppm) compositions of BIF from Dujiagou.

Sample	51-1	51-2	61-1	61-2	71-1	71-2	81-1	81-2	2018-1-1	2018-1-2	2018-2	PM040-37-1	D5216-2	Sijiaying	Hamersley	Itilliarsuk	Um Anab	Nkout
Magnetite quartzite														**Average**				
SiO_2	56.00	54.56	55.95	54.55	56.12	54.39	63.47	63.42	55.90	54.70	63.67	39.75	55.04	55.88	50.35	47.37	54.62	46.93
TiO_2	0.09	0.03	0.08	0.03	0.09	0.04	0.12	0.12	0.08	0.03	0.11	0.04	0.09	0.01	0.09	0.18	0.20	0.11
Al_2O_3	0.89	0.82	0.88	0.83	0.87	0.82	1.28	1.28	0.93	0.87	1.31	0.50	0.88	0.47	2.14	3.78	3.60	3.38
TFe_2O_3	38.63	40.32	38.67	40.30	38.76	40.20	29.39	29.14	37.53	39.30	28.30	55.37	35.91	41.76	41.71	44.61	35.14	44.54
MnO	0.27	0.24	0.27	0.24	0.27	0.23	0.29	0.29	0.28	0.24	0.30	0.07	0.23	0.05	0.07	0.06	0.07	0.12
MgO	3.33	2.43	3.35	2.41	3.32	2.42	2.03	2.01	3.27	2.33	1.96	1.37	3.15	0.67	1.86	0.95	1.28	2.47
CaO	1.42	0.53	1.43	0.53	1.43	0.53	1.92	1.90	1.39	0.50	1.88	0.58	1.28	0.43	1.79	1.99	2.98	1.59
Na_2O	0.15	0.06	0.13	0.05	0.17	0.08	0.14	0.09	0.16	0.05	0.09	0.02	0.11	0.13	0.14	0.57	0.25	0.24
K_2O	0.13	0.12	0.12	0.13	0.12	0.12	0.14	0.13	0.16	0.05	0.09	0.03	0.09	0.06	0.18	0.25	0.12	0.96
P_2O_5	0.24	0.18	0.24	0.18	0.24	0.18	0.45	0.45	0.25	0.18	0.45	0.32	0.25	0.07	0.22	0.23	0.54	0.09
LOI	-1.15	0.32	-1.13	0.25	-1.21	0.20	0.73	0.89	-0.96	0.55	1.12	1.08	1.84	0.47	2.22	-	0.53	-0.27
FeO	23.40	12.25	23.80	12.20	23.50	11.60	7.75	7.55	23.80	12.71	8.08	16.22	25.40	9.58	-	-	-	-
Sc	3.85	3.05	3.59	3.02	3.67	3.02	5.32	5.31	3.40	2.60	4.80	1.50	2.93	0.85	2.80	5.54	6.20	-
V	19.69	10.88	18.83	10.96	19.19	11.41	45.19	44.70	24.00	13.00	54.00	16.50	26.10	12.74	19.78	-	77.80	1.10
Cr	56.28	33.62	53.88	34.57	53.54	34.17	104.13	103.59	70.00	50.00	130.00	24.10	80.30	647.14	203.47	25.04	26.60	6.46
Co	118.76	110.74	111.75	112.65	111.01	112.29	144.17	142.72	115.00	112.50	143.50	2.45	9.89	4.78	4.49	-	95.50	0.25
Ni	36.98	49.25	35.58	50.51	35.15	50.83	102.63	101.90	40.50	53.50	103.50	14.40	42.00	21.74	-	17.36	10.67	1.01
Ga	4.58	2.45	4.44	2.52	4.53	2.52	11.07	10.64	4.70	2.70	11.50	4.46	4.15	1.81	-	-	-	-
Rb	3.18	8.59	3.27	8.80	3.15	8.65	7.61	7.49	3.40	9.00	8.20	4.70	4.20	5.68	-	3.09	3.60	8.06
Sr	11.41	5.36	11.16	5.66	11.06	5.43	10.66	10.71	11.90	5.80	11.40	8.80	7.08	29.59	-	85.27	147.80	1.28
Y	25.34	15.28	24.97	15.74	24.73	15.62	39.65	39.44	25.00	15.60	38.60	17.80	19.90	4.78	12.41	3.26	26.60	0.27
Zr	7.31	5.09	7.17	5.25	6.62	5.52	11.70	14.43	7.00	6.00	16.00	3.82	7.37	2.5	32.94	29.63	44.50	0.00
Nb	3.67	2.03	3.52	2.02	3.50	2.04	7.23	7.06	3.70	2.00	7.50	2.88	2.38	0.36	-	-	2.38	0.00
Ba	145.24	151.29	149.99	152.32	143.30	152.12	148.88	147.57	151.50	157.50	150.00	40.40	36.50	18.13	75.67	-	64.90	34.69
La	6.37	9.58	6.25	9.73	6.06	9.70	11.98	11.58	6.70	10.10	13.50	7.30	9.75	3.12	8.14	3.24	12.13	0.67
Ce	13.98	26.88	13.80	27.70	13.46	27.16	37.51	37.12	16.80	27.00	39.80	15.90	17.50	4.97	14.54	8.88	27.09	1.21

Pr	2.07	2.77	2.06	2.79	2.02	2.80	5.10	5.07	2.15	2.87	5.38	1.84	2.31	0.65	1.71	0.80	3.78	0.13
Nd	9.37	11.35	9.51	11.33	9.37	11.53	24.20	24.35	9.50	11.60	23.60	10.00	11.90	2.71	6.50	3.23	16.58	0.44
Sm	2.82	3.10	2.66	2.94	2.67	3.09	7.29	7.12	2.71	2.81	6.93	2.59	2.94	0.54	1.23	0.65	3.98	0.06
Eu	0.64	0.63	0.70	0.63	0.67	0.65	1.65	1.59	0.71	0.66	1.58	0.50	0.74	0.16	0.30	0.22	1.05	0.02
Gd	3.18	2.99	3.53	3.08	3.28	2.97	7.41	7.27	3.37	3.12	7.46	2.74	2.99	0.61	1.30	0.29	4.65	0.05
Tb	0.59	0.48	0.62	0.53	0.55	0.51	1.16	1.20	0.56	0.48	1.19	0.49	0.54	0.1	0.21	0.11	0.75	0.00
Dy	3.90	2.99	3.92	3.14	3.93	3.12	7.58	7.49	3.65	2.81	6.94	3.18	3.56	0.63	1.34	0.63	4.67	0.04
Ho	0.86	0.62	0.80	0.61	0.82	0.60	1.44	1.49	0.82	0.58	1.42	0.70	0.79	0.15	0.34	0.12	1.06	0.01
Er	2.36	1.63	2.39	1.68	2.35	1.63	3.91	3.91	2.36	1.59	3.77	1.90	2.22	0.43	1.05	0.35	3.19	0.02
Tm	0.35	0.25	0.36	0.26	0.36	0.24	0.56	0.55	0.36	0.25	0.59	0.30	0.37	0.06	0.16	0.05	0.47	0.00
Yb	2.30	1.68	2.35	1.71	2.34	1.70	3.63	3.51	2.36	1.63	3.71	1.90	2.54	0.42	1.13	0.31	3.19	0.02
Lu	0.36	0.27	0.39	0.27	0.37	0.27	0.57	0.55	0.38	0.27	0.59	0.26	0.36	0.07	0.19	0.05	0.50	0.00
Hf	0.26	0.18	0.33	0.17	0.26	0.19	0.52	0.58	0.20	0.20	0.50	0.18	0.34	0.09	0.85	0.82	0.68	0.00
Ta	0.23	0.14	0.25	0.15	0.25	0.14	0.64	0.62	0.21	0.12	0.54	0.07	0.12	0.05	-	-	1.38	-
Pb	1.18	8.27	1.33	8.29	1.19	7.91	7.87	7.96	1.10	6.70	7.30	42.60	14.30	3.55	8.91	2.69	7.00	0.18
Th	0.70	0.51	0.61	0.53	0.64	0.53	1.12	1.14	0.60	0.51	1.22	2.92	3.61	0.31	2.26	0.49	1.85	0.11
U	0.48	0.53	0.47	0.54	0.47	0.54	0.81	0.85	0.46	0.49	0.87	0.40	0.37	0.26	0.86	0.32	0.40	0.07
ΣREE+Y	74.49	80.52	74.31	82.15	72.98	81.59	153.62	152.24	77.43	81.37	155.06	67.40	78.41	19.4	50.55	22.19	109.69	3.12
(La/Yb)$_{PAAS}$	0.20	0.42	0.20	0.42	0.19	0.42	0.24	0.24	0.21	0.46	0.27	0.28	0.28	0.59	0.53	-	0.29	7.16
La/La*	1.48	1.11	1.67	1.11	1.65	1.14	1.52	1.63	1.35	1.10	1.05	-40.23	7.35	1.34	1.11	1.33	-	-
Pr/Pr*	1.00	0.90	0.98	0.89	0.99	0.90	0.94	0.93	0.95	0.92	0.98	0.81	0.88	1.04	1.00	-	1.03	0.94
Ce/Ce*	0.87	1.19	0.87	1.22	0.87	1.19	1.06	1.06	1.01	1.15	1.04	1.00	0.85	0.8	0.89	1.63	0.91	0.93
Eu/Eu*	0.99	0.97	1.04	0.97	1.03	1.00	1.04	1.03	1.07	1.03	1.02	0.87	1.16	1.41	2.48	1.63	1.16	1.81
Y/Ho	29.59	24.55	31.25	25.64	30.21	25.90	27.55	26.51	30.49	26.90	27.18	25.43	25.19	31.64	36.50	26.86	25.10	34.04

240   La/La*=La$_{PAAS}$/(3Pr$_{PAAS}$-2Nd$_{PAAS}$); Ce/Ce*=2Ce$_{PAAS}$/(La$_{PAAS}$+Pr$_{PAAS}$); Eu/Eu*=2Eu$_{PAAS}$/(Sm$_{PAAS}$+Gd$_{PAAS}$); Pr/Pr*=2Pr$_{PAAS}$/(Ce$_{PAAS}$+Nd$_{PAAS}$) (Bolhar et al., 2004). BIF data of Sijiaying are from Wang et

241   al. (2017); BIF data of Hamersley are from Warchola et al. (2018) ; BIF data of Itilliarsuk are from Haug Aa Rd et al. (2013); BIF data of Um Anab are from Basta et al. (2011). BIF data of Nkout

242   West are from Ndime et al. (2019).

4. Results

4.1. Zircon U-Pb ages

The mostly sub-angular to sub-rounded zircon grains from the metamorphic mafic rock in the Yemadong Complex are 80-150 μm in length, with length/width ratios of 1-1.5 (**Figure 3**). Cathodoluminescence images show that the light gray, moderately rounded zircons commonly lack oscillating zonations, and that they possess core morphological characteristics suggestive of metamorphic zircons. The LA-ICP-MS ages for 45 zircon grains with single point analyses are displayed in **Table 1**. Ten with abnormally high Eu content and four with anomalously high U concentrations were omitted from the age calculation. Thirty-one of the forty-five grains were successfully dated and plotted on the concordia diagram shown in **Figure 3a**. Their U zircon concentrations varied from 323-1094 ppm and Th from 38.1-140 ppm, with Th/U ratios doubling from 0.09-0.18 (**Table 1**). Seventeen analyses formed a coherent group on the concrodia line (**Figure 3b**), yielding a weighted $^{206}Pb/^{207}Pb$ mean age of 2901 ± 8 Ma (MSWD = 0.77, **Figure 3c**). Forteen points formed a discord stretched between the seventeen previously mentioned points, with an upper and lower $^{206}Pb/^{238}U$ age intercept of 2909 ± 14 Ma and 775 Ma (MSWD =1.5), respectively (**Figure 3a**). The obtained 1063.6 ± 3.6 Ma concordia age for 20 samples, corresponded with the $^{207}Pb/^{235}U$ age of 1063.5 ± 7.3 Ma measured for the 91500 zircon standard, is within analytical uncertainty, and agrees well with the more robust ID-TIMS $^{207}Pb/^{235}U$ age of 1065.4 ± 0.3 Ma (Jackson et al., 2004).

262

263
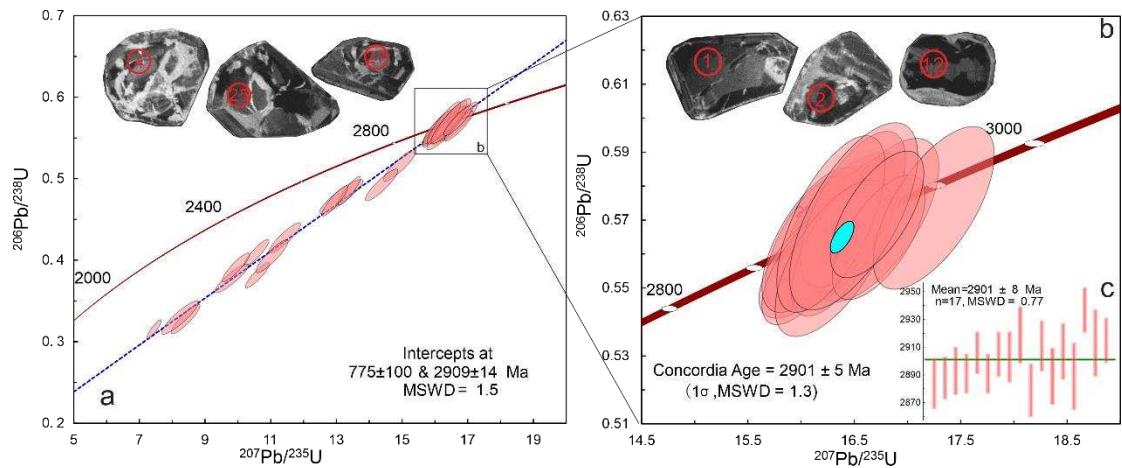
Figure 3. Zircon U-Pb concordia diagrams and their representative cathodoluminescence images from the Dujiagou

BIF samples. Red circles indicate the location of the laser ablation spots. Each spot location is labeled by analysis

number.

4.2. Bulk-rock geochemical compositions

The silicon-rich and iron-rich layers display typical characteristics typical of Archean BIF,

composed mainly of 39.75-63.67 wt.% SiO_2 and 28.30-55.37 wt.% TFe_2O_3. Al_2O_3, MgO, TiO_2 and

CaO contents range from 0.50-1.31 wt.%, 1.37-3.35 wt.%, 0.03-0.12 wt.% and 0.50-1.92 wt.%,

respectively, suggest a degree of terrigenous detrital contamination (**Table 2**). The samples contain

low K_2O, Na_2O, MnO and P_2O_5 concentrations averaging 0.11, 0.10, 0.25, and 0.28 wt.%,

respectively concentrations, being generally compatible with the major element content of Early

Precambrian BIF (**Table 2**, **Figure 4**).

275
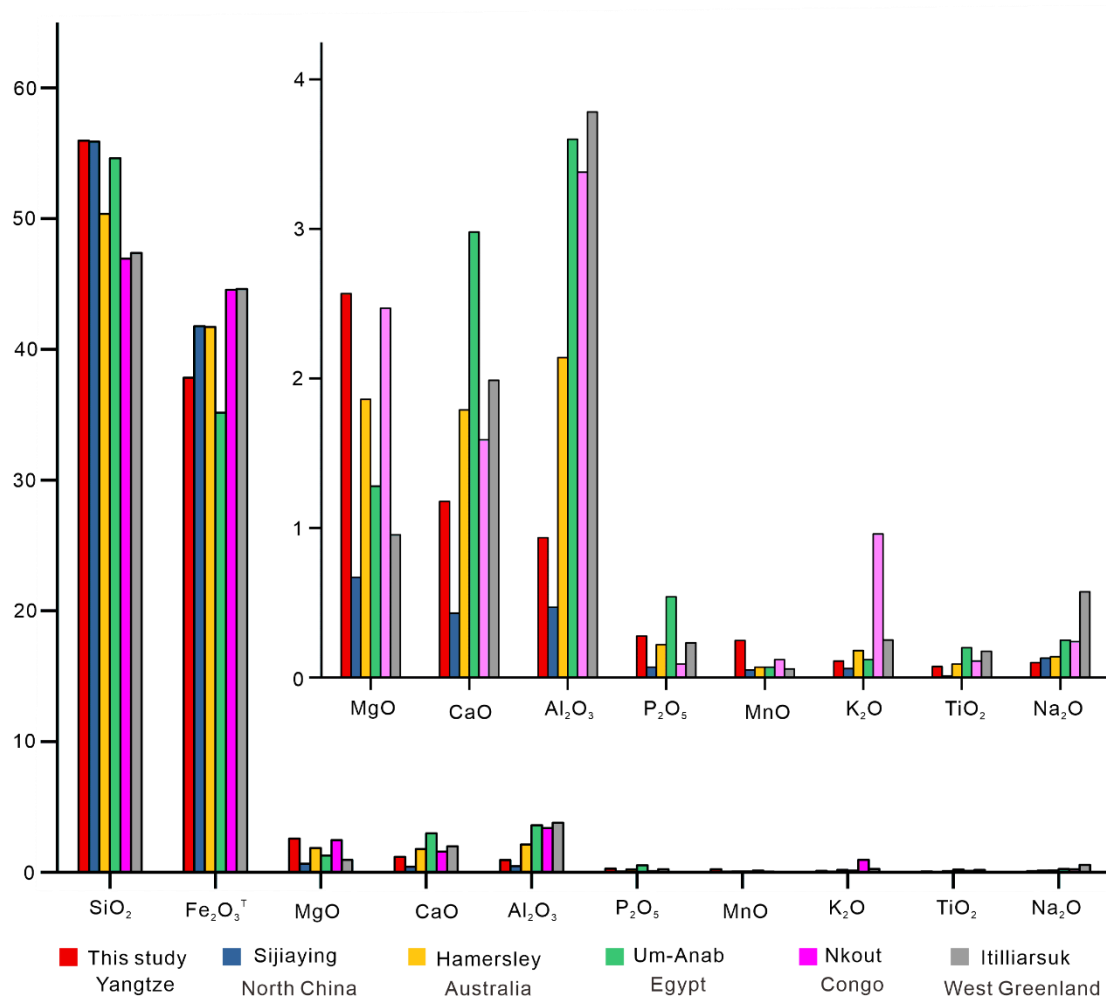
Figure 4. Mean values of major elements in the Dujiagou BIFs and early Precambrian BIFs from other areas. BIF data are from **Table 2**.

The samples display a wide range in incompatible element content, with Zr, Hf, Sc, and Th occurring in high concentrations of 3.82-16 ppm, 0.17-0.58 ppm, 1.5-5.32 ppm, and 0.51-3.61, respectively. Their high abundance not encountered in Archean and Paleoproterozoic detritus-free BIFs, support terrigenous contamination (e.g., Li et al. (2012b); Wang et al. (2017), **Table 2**). Total REE + Y average 94.74 ppm and range from 67.40-155.06 ppm (**Table 2**). Post Archean Average Shale (PAAS) normalized REY patterns are characterized by the depletion of light REE relative to heavy REE, $(La/Yb)^* = 0.19$-0.46, with an average of 0.30. Calculated Eu/Eu^* values varying from 0.87-1.12, point to positive and negative Eu anomalies across the sedimentary suite, while Ce/Ce^* values of 0.85-1.22 suggest Ce anomalies are muted across the sequence. The La/La^* values of 1.05-

288   7.35 and averaging 1.85, indicate a sample set characterized by moderate positive La anomalies

289   (**Table 2**). Thirteen samples are significantly enriched in Y relative to Ho, yielding chondritic or

290   suprachondritic Y/Ho ratios 24.55-31.25, with an average of 27.41. The Dujiagou BIFs show

291   remarkably weaker positive or negative Eu^* anomalies and higher $\sum REY$, which are significantly

292   different from the average of most Archean BIFs (**Table 2**).

293   **4.3. Fe isotopic composition**

294   The $\delta^{56}Fe_{IRMM-014}$ of magnetite from seven samples are enriched in heavy Fe isotopes, with a

295   range of 0.25-0.45 ‰ and an average 0.35 ‰. These values are similar to standard $\delta^{57}Fe_{IRMM-014}$

296   values of 0.37-0.68 ‰ that average 0.52 ‰ (**Table 3**). The $\delta^{56}Fe_{IRMM014}$ values of 0.110 ± 0.048 ‰

297   and $\delta^{57}Fe_{IRMM014}$ of 0.166 ± 0.080 ‰ (n=12) for AVG-2 measured here overlap with newly

298   recommended Isoplot values ([Ludwig, 2000](#)) reported by ten independent laboratories

299   ($\delta^{56}Fe_{IRMM014}$=0.110 ± 0.048 ‰, $\delta^{57}Fe_{IRMM014}$=0.141 ± 0.005 ‰ ([He et al., 2015](#)).

300   **Table 3**. Fe isotope compositions for BIFs representatives from the Dujiagou Formation

Sample no.	Object (Whole rock)	$\delta^{56}Fe_{IRMM-014}$ (‰)	2σ	$\delta^{57}Fe_{IRMM-014}$ (‰)	2σ	$\delta^{57/56}Fe_{IRMM-014}$ (‰)	2σ
Ibr 1-1a	BIF	0.45	0.0252	0.65	0.0411	0.20	0.0349
Ibr 1-1b	BIF	0.45	0.0306	0.69	0.0371	0.22	0.0268
Ibr 1-1c	BIF	0.45	0.0281	0.65	0.0446	0.22	0.0332
Ibr 2-2a	BIF	0.27	0.0254	0.44	0.0372	0.17	0.0262
Ibr 2-2b	BIF	0.29	0.0262	0.44	0.0365	0.14	0.0327
Ibr 2a	BIF	0.27	0.0276	0.43	0.0390	0.14	0.0274
Ibr 2b	BIF	0.25	0.0227	0.37	0.0406	0.11	0.0360

301

302   **5. Discussion**

303   **5.1. Metamorphic transformation and age of the Dujiagou BIFs**

304   Previous compilations of zircon Th/U ratios led to the proposition of a general Th/U threshold

305   value of 0.1 to differentiate between metamorphic and igneous zircon ([Rubatto, 2017](#)). Based on the

new compilation of zircon analyses from Western Australia, igneous zircons rarely possess Th/U

ratios of <0.1 while those of metamorphic zircons range between <0.01 and >10. Therefore, zircons

with Th/U ratios <0.1 are more likely to be metamorphic, and those with Th/U ratios >0 of either

igneous or metamorphic origin. However, it has been proposed that a Th/U ratio = 0.4 is more

suitable for distinguishing metamorphic rocks from igneous rocks (Yakymchuk et al., 2018).

Because Th^{4+} has a larger ionic radius than U^{4+}, it exhibits a weaker stability than U in the zircon

lattice, and is easier to expel from the zircon lattice during metamorphic recrystallization, resulting

in a relatively lower Th/U ratio in recrystallized metamorphic zircons (Hoskin and Black, 2000).

Among the thirty-two zircons successfully dated in this study, six revealed Th/U≤0.1 and the

remaining twenty-six had 0.1<Th/U≤0.18, which collectively suggests that the Th/U ratios of all

the studied zircons fell within the expected metamorphic range. In addition, cathodoluminescence

imaging, such as metamorphic accretion edge (**Figure 3a, b**), support the metamorphic genesis of

the zircons.

Previous studies have shown that the TTG suites in the Kongling terrane were formed at ~3.0-

2.90 Ga (Qiu et al., 2000; Zhang et al., 2006; Zheng et al., 2006; Gao et al., 2011; Kang et al., 2013;

Qiu et al., 2018; Wei et al., 2019; Wei, 2021). However, the xenoliths in the TTG of the Kongling

terrane show an older age of 3.2-3.0 Ga (**Table 4**). Significant tecto-thermal activity between 3.2

and 3.0 Ga in the Yangtze Craton, formed the HGB (**Table 4**)—a typical Archean greenstone belt

(Wei and Wang, 2012; Wei and Jing, 2013; Wei et al., 2020; Wei, 2021). The 3.0-2.9 Ga TTG plutons

intruded and split the greenstone belt into separate greenstone remnants or septa, leading to the

cropping out of these HGB residues as enclaves of ~10 cm to 20 m thick within the younger TTG

gneisses (Gao and Zhang, 1990; Xiong et al., 2004; Li et al., 2014b; Guo et al., 2015; Wei et al.,

328 2020; Wei, 2021). In the Kongling area, more than 96% of the HGB is invaded and covered by the

329 Mesoarchean TTG gneiss, with a total sporadic exposure area of ~ 6 km^2 (Wei, 2021). In this study,

330 we obtain an average weighted ^{206}Pb/^{207}Pb Mesoarchean age of 2901±8 Ma from the metamorphic

331 zircons recovered from the metamorphosed mafic rocks interbedded with the thin Dujiagou BIFs.

332 The layer thickness of these rocks is uniform, being regularly repetitive in the vertical section

333 (**Figure 2a-c**), which may represent intermittent volcanic activity, and the BIFs moments quiescent

334 volcanic activity. Therefore, the interlayered metavolcanic mafic rocks can be considered

335 contemporaneous with the Dujiagou BIFs (Zhang et al., 2012), and the mafic volcanic rocks form

336 the HGB (Wei et al., 2019; Wei et al., 2020; Wei, 2021). In this paper, since all the zircons underwent

337 strong metamorphism, we interpret the ^{206}Pb/^{207}Pb age of 2901±8 Ma as the metamorphic age

338 related to the same thermal tectonic event at ~2.95-2.90 Ga recorded by the aforementioned mafic

339 volcanic rocks, while the deposition of the Dujiagou BIFs occurred prior to the inferred

340 metamorphic event. Since it is difficult to observe the actual extent and full cross section of the

341 HGB, the sampled outcrop probably represents only a limited exposure, true thickness and size of

342 the Dujiagou BIFs. For example, in the Pitangui greenstone belt, exposed BIF outcrops consist of

343 both thin and extremely thick layers with >10 times thickness difference along the cross section

344 (Brando Soares et al., 2017). Regardless of actual size and thickness, the data suggest that the

345 Dujiagou BIFs are the oldest known deposit in the Yangtze Craton.

346

347

348

Table 4. Compilation of isotopic ages of xenoliths in TTG suite of Kongling terrane in Huangling region

Sample location	Lithology /xenoliths	Protolith	Sample number Rock/Zircon	Age (Ma)	Method
Yemadong (this study)	metavolcanic mafic rocks	volcanic mafic rocks	31 (zircon)	2901±8	Zircon U-Pb LA-ICP MS
①Yemadong	Miotite–tremolite schist	Basic igneous rock	41 (zircon)	3011±27, 2933±13	Zircon U-Pb LA-ICP MS
②Yemadong	Massive amphibolite	Tholeiitic basalt	15 (zircon)	3000 ± 24	Zircon U-Pb LA-ICP MS
③Wangjiatai	Banded amphibolite	Tholeiitic basalt	6 (zircon)	3242 ± 140	Zircon U-Pb LA-ICP MS
④Hetaoyuan	Banded amphibolite	Komatiitic/Tholeiitic basalt	4 (zircon)	3013 ± 23	Zircon U-Pb LA-ICP MS
⑤Hetaoyuan	Amphibole schist	Komatiitic/Tholeiitic basalt	7 (whole-rock)	2998.9	Sm-Nd isochronIsotope
⑥Dongping	Banded amphibolite	Tholeiitic basalt	13 (whole-rock)	3290 ± 170	Sm-Nd isochronIsotope

The given ages are from ①Wei et al. (2019); ②Wei and Wang (2012); ③Wei et al. (2020); ④–⑤Wei and Jing (2013); ⑥Ma et al. (2002), respectively.

5.2. Elemental geochemistry

Castic contamination, minor amounts of crustal material are sufficient to obscure original marine signatures if not carefully constrained (Bau, 1993; Bolhar et al., 2004). For instance, contamination with terrigenous detrital induces elevated and false correlated abundance of incompatible elements (Th, Hf, Zr, Sc, etc.) (Bolhar et al., 2004). BIF samples yielding high abundance of immobile trace elements (for example Sc > 2 ppm) should be excluded from a debris-free sample set (Bau, 1993) and high abundances of immobile trace elements such as 1.50-5.32 ppm Sc, 0.51-3.61 ppm Th, 3.82-16.0 ppm Zr, and 0.17-0.58 ppm Hf, confirm detrital incorporation. These values are about an order of magnitude higher than for the debris-free BIF samples (e.g., Li et al. (2012b) and Wang et al. (2017)). Crustal components are rich in Th (Zhao and Zhou, 2007), and therefore an R^2=0.88 supported positive correlation between Th and Zr (**Figure 5a**). This co-variation indicates that the Dujiagou BIFs were contaminated by detrital material. In addition, a

strong positive correlation between Al_2O_3 and TiO_2 is often interpreted to reflect the incorporation

of detrital components in sedimentary rocks, and therefore widely used as a proxy for detrital

contamination of chemical sediments (e.g., Basta et al. (2011).The moderate positive correlation

between Al_2O_3 and TiO_2 in the Dujiagou BIFs with r value of 0.76 (**Figure 5b**) is therefore consistent

with detrital input from the weathering of existing continental landmass. Although fairly low, the

0.54 -1.42 wt.% Al_2O_3 + TiO_2 content of the Dujigou BIFs, are largely higher than for pristine

examples of Algoma-type BIFs (e.g., Wang et al. (2017)). The discovery of a small amount of

amphibole and other accessory minerals in the Dujiagou BIFs provide further strong evidence of

terrigenous debris contamination (**Figure 2f**).
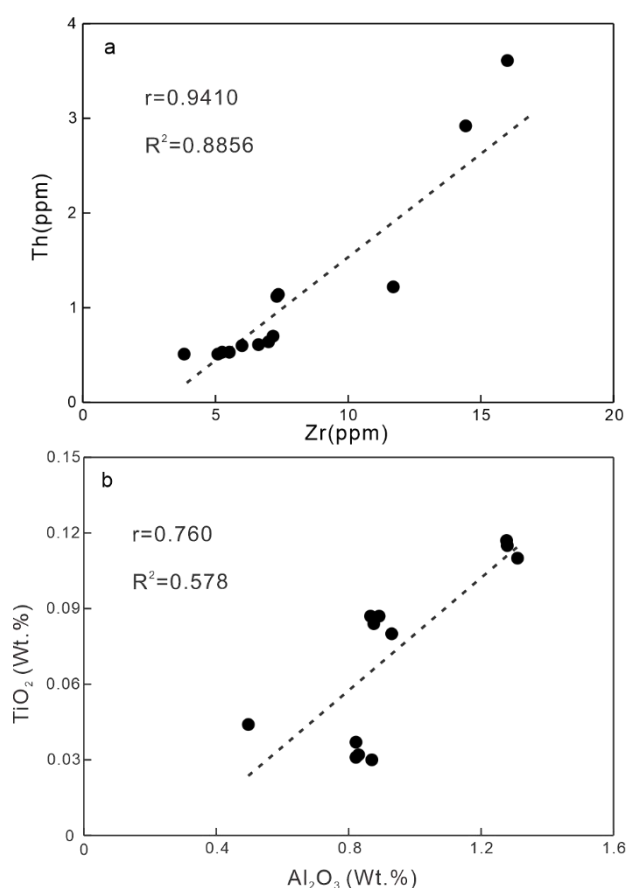
Figure 5 Discrimination diagrams for major and trace elements in the Dujiagou BIF, Hangling region, Yangtze Craton, (a) Zr vs. Th and (b) Al_2O_3 vs. TiO_2.

5.3. Sources of iron and silica

The sources of iron in BIFs is debated, with hydrothermal fluids (Basta et al., 2011; Wang et al., 2017) or a mixture of both hydrothermal and terrigenous supply suggested (Pecoits et al., 2009; Li et al., 2015). Also, as a remnant of HGB, the metamorphic amphibolite xenoliths believed to have originated from a tholeiitic protolith (Wei, 2021), show distinct positive correlation between Al_2O_3 and TFe_2O_3 ($R^2 = 0.84$). To the contrary, the strong negative correlation ($R^2 = 0.91$) between Al_2O_3 and TFe_2O_3 (**Figure 6a**), precludes the sourcing of Fe from the continent or derived by detrital contribution. Generally, diagenesis and various post-depositional processes, including hydrothermal alteration, could strongly affect the mobility of redox-sensitive elements, e.g., when Eu anomalies arise from the reduction of Eu (III) to Eu (II) (Bau, 1993). Previous studies have documented that REEs are largely immobile during low-grade metamorphism, e.g., in amphibolite facies (Finger et al., 1998; Huang et al., 2014), and that the mineral reactions that occur during prograde metamorphism of BIF are essentially isochemical, except for decarbonation and dehydration (Klein, 2005). The amphibolite metamorphism experienced by the Dujiagou BIF may therefore be insignificant with respect to impact on the migration and enrichment of REEs.

The geochemical characteristics of ancient oceans and hydrothermal fluids are often inferred from the compositions of modern seawater and seafloor hydrothermal fluids (Bolhar et al., 2004; Bolhar and Vankranendonk, 2007). Typically, when normalized to PAAS, REY patterns for the modern seawater are enriched in HREE relative to LREE. They are characterized by no Eu anomalies and a strong negative Ce anomaly typifies modern oxygenated seawater (**Figure 6b**). Further, high-temperature (>250℃) hydrothermal fluids contain pronounced positive Eu anomalies, whereas a weak or no Eu anomaly characterizes low-temperature (<250℃) hydrothermal fluids

(**Figure 6b**). Therefore, the Eu anomaly has become a mainstream proxy for identifying the material source of Precambrian BIFs. When normalized to PAAS, the Dujiagou BIFs ΣREY_{PAAS} patterns are different from typical Precambrian debris-free IFs. For example, they are much higher, with several samples having element/PAAS ratios close to or above 1. Also, they contain extremely faint Eu and Ce positive anomalies, and the curves are much flatter than observed for pristine BIFs (**Figure 6c**). The lack of positive Eu anomalies in our samples is inconsistent with most Archean BIFs that tend to have strong positive Eu anomalies. Interestingly, the strong positive correlation ($R^2 = 0.83$) between Al_2O_3 and ΣREY (**Figure 6d**), suggest that the slightly positive Eu anomalies are indicative of the dilution of a high-temperature hydrothermal source of the BIFs by detrital material (Yang et al., 2022). Nonetheless, the positive Eu anomalies observed in the Dujiagou BIFs are consistent with those recorded for world-wide BIF deposits of the same age, attributed to a hydrothermal provenance. It is thus possible that terrigenous contamination did not completely erase the primary hydrothermal REE signal, in which case the observed positive Eu anomalies may in fact be pointing to the hydrothermal source of the Dujiagou BIFs. Moreover, the geochemical characteristics of biotite-tremolite schist enclaves from the Yemadong Complex are similar to those of island arc volcanic deposits (Wei et al., 2019), leading to the conclusion that the Dujiagou BIFs and their host volcanic rocks were developed in an island arc setting as opposed to a shelf environment, similar to Algoma-type BIFs. The Dujiagou BIFs are intimately associated with volcanic rocks, therefore, the hydrothermal activity that formed them is considered to be associated with volcanism, suggesting that the insignificant Eu anomalies are unlikely to be of low-temperature hydrothermal origin. Furthermore, BIFs of low-temperature hydrothermal origin appear to be mainly a feature of the Neoproterozoic (e.g., Basta et al. (2011); Yang et al. (2022)).
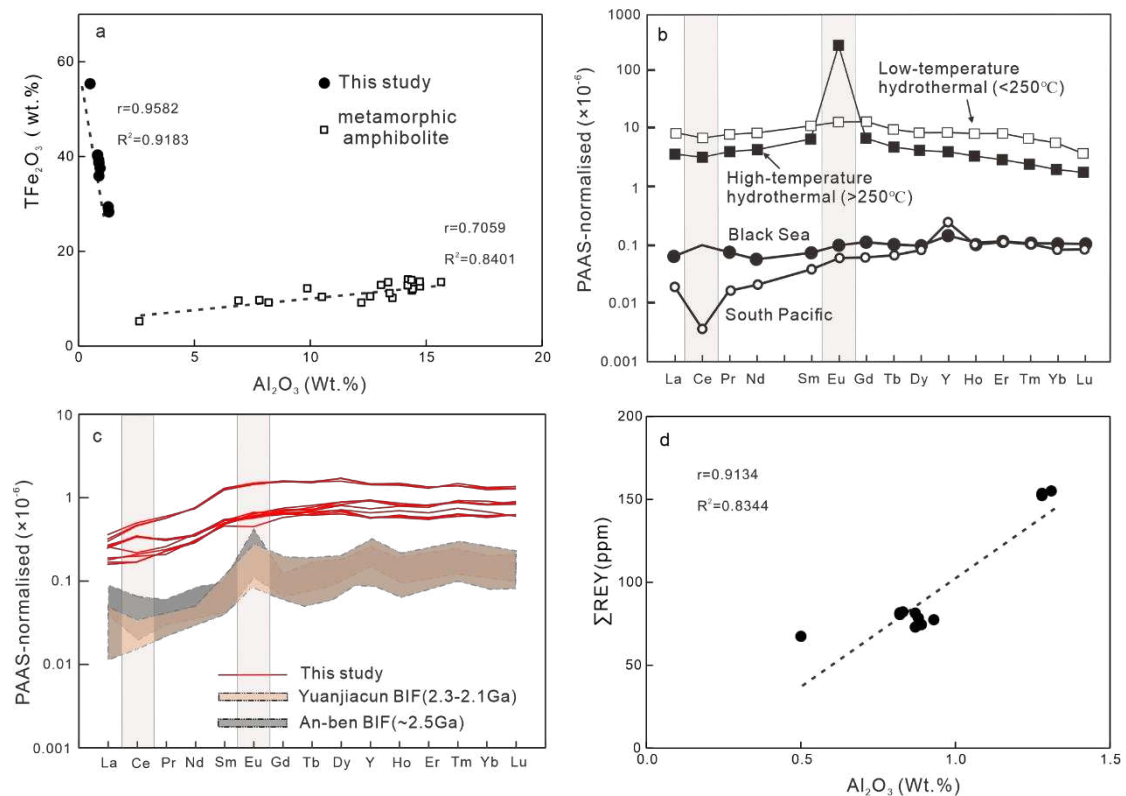
Figure 6. Discrimination diagrams for major and trace elements (a) Relationship between Al_2O_3 and TFe_2O_3 in the Dujiagou BIF and metamorphic amphibolite xenoliths (Wei, 2021), Hangling region, Yangtze Craton, (b) South Pacific ocean oxygenated modern seawater, the modern Black Sea anoxic seawater, and Eu anomaly of modern high and low-temperature marine hydrothermal fluids (Bolhar and Vankranendonk (2007) and references therein), (c) PAAS-normalized REE + Y diagrams of the relationships between REEs and different BIF types. Yuanjiacun Superior-type BIF data from Wang et al. (2014); An-ben Algoma-type BIF data from Li et al. (2012b), and (d) Relationship between Al_2O_3 and $\sum REY$ in the Dujiagou BIF.

The Y/Ho ratio of BIFs are also widely used to interpret the source of ore-forming materials and sedimentary settings, e.g., Basta et al. (2011); Viehmann et al. (2014); Wang et al. (2017). The Blundy and Wood model (Blundy and Wood, 1994) suggests that in comparison to the degree of fractionation within the REE series, Y-Ho fractionation should be minor to negligible, and even more evolved melts do not readily fractionate Y from Ho (Bau and Dulski, 1996). Although Y and

436   Ho share similar geochemical properties they are fractionated differentially in seawater (Nozaki et

437   al., 1997). In the modern oxidized ocean, where hydrothermal fluids mix with seawater near vent

438   orifices, Y concentrations are conservative. On the contrary, REEs from the hydrothermal fluids are

439   partially adsorbed by precipitating Fe-oxyhydroxides when Fe^{2+} begins to rapidly oxidize to Fe^{3+}

440   immediately after release from the vents, producing a large decrease in sedimentary Y/Ho ratios

441   relative to seawater (Bau and Dulski, 1999). Chondritic Y/Ho ratios average ~28 (Sun and

442   McDonough, 1989), while seawater is characterized by superchondritic ratios of 44-47 (Bau and

443   Dulski, 1999). Although the Y/Ho ratio for rivers and estuaries fall between seawater and continental

444   rocks values, experiments have shown that fractionation in river and estuarine systems is negligible,

445   with little influence on the relative abundance of Y and Ho in the ocean (Nozaki et al., 1997). Y/Ho

446   ratios in the Dujiagou BIFs range from 24.6 to 31.3, with an average of ~27.4 being closer to

447   chondritic values, but far lower than modern seawater ratios. However, small admixtures of any

448   contaminant would depress seawater-like Y/Ho ratios (Bau and Dulski, 1999). The high Zr content

449   in BIFs samples has been confirmed as a source of terrigenous debris input, and the Y/Ho ratios

450   show a negative correlation with Zr (R^2 = 0.18, **Figure 7**). Therefore, the real Y/Ho ratio is

451   considered affected by terrigenous debris, thus presenting the illusion of a relatively low average

452   Y/Ho ratio. Although terrigenous debris reduces the Y/Ho ratio, four of the BIF samples contained

453   superchondritic ratios, consistent with a hydrothermal origin. In summary, the origin of the Dujiagou

454   BIFs is considered to be more closely related to a hydrothermal source rather than terrigenous debris.
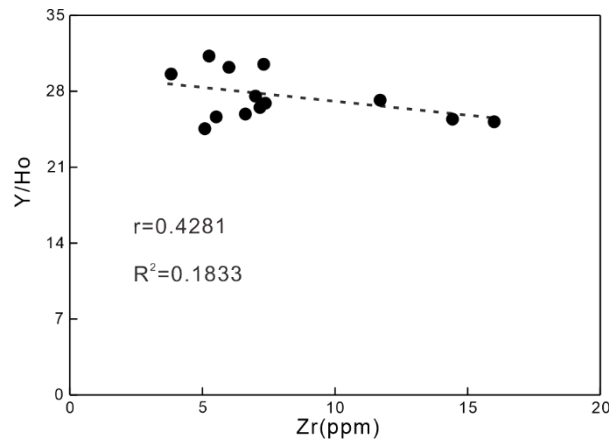
Figure 7. Plots of a Zr vs. Y/Ho in the Dujiagou BIF, Hangling region, Yangtze Craton.

5.4. Sedimentary environment

5.4.1. Rare Earth Elements (REE)

In general, anoxic and suboxic waters lack large negative Ce anomalies when normalized to PAAS, while oxygenated marine seawater displays a strong negative Ce anomaly (**Figure 6b**). In some cases, abnormal La enrichment may cause non-redox-dependent Ce depletion. As a consequence, Bau and Dulski (1996) proposed to use Ce/Ce^* vs. Pr/Pr^* cross plots to identify La and Ce anomalies in BIFs (**Figure 8a**). In **Figure 8a,** six BIF samples plot within positive Ce anomalies, which is generally not considered a predominant feature of chemical sediments precipitated from Archean seawater (Bolhar et al., 2004). The most likely cause is debris contamination, just as the Eu anomalies in the same batch of samples suggest. We are therefore inclined to consider the Ce anomalies as potentially unreliable tracers of the redox conditions in which they formed. Nonetheless, the lack of negative and true Ce anomalies is consistent with the expected anoxic waters of the Archean Ocean.

5.4.2. Iron isotopes

5.4.2.1. Iron isotopes and metamorphic influences

Given the fact that the Dujiagou BIFs have been metamorphosed, as shown by different lines of evidence, to amphibolite grade metamorphism, it is necessary to evaluate the influence of metamorphism on the studied iron isotopes before they are used for geochemical interpretative purposes. Based on studies on the Paleoproterozoic Biwabik iron formation, Hyslop et al. (2008) showed that metamorphism can altered the primary isotopic composition of O atoms in quartz and magnetite and iron in magnetite and iron silicate minerals. The self-diffusion coefficient of Fe in magnetite at a metamorphic temperature of 500 °C depends on the activity of O_2, but is greater than $\sim10^{-16}$cm^2/s (Atkinson et al., 1983), with a corresponding diffusion length of $\sim$1 mm (Dauphas et al., 2007a). In this case, $\sim$ 3 Ma is required for complete diffusion of iron isotopes over an average length of 2 mm (Czaja et al., 2013). However, the diffusion of iron isotopes can only occur in individual iron layers, because magnetite bands are separated by quartz bands, which would be an effective barrier to iron diffusion. In the hand samples, it seems unlikely that large-scale transport of iron occurred during metamorphism and the overall average $\delta^{56}Fe_{Mt}$ values are likely to be reflective of those of the original BIF sediment (Czaja et al., 2013). The independent study of the $\sim$1.8 Ga Biwabik BIFs shows that metamorphism could slightly reduce the $\delta^{56}Fe_{Mt}$ in BIFs, but that metamorphism cannot explain the positive $\delta^{56}Fe_{Mt}$ measured in BIFs, including Archean BIFs (Hyslop et al., 2008). Consequently, Fe isotopic composition of magnetite is much less affected by metamorphism compared to other mineral phases (Dauphas et al., 2007a; Hyslop et al., 2008). Moreover, it is has been proposed that the iron isotopic composition of BIFs are not involved in amphibolite facies metamorphism after formation (Dauphas and Rouxel, 2006; Frost et al., 2006;

494   Dauphas et al., 2007a; Czaja et al., 2013). We therefore assume that the iron isotopic composition

495   of the Dujiagou BIFs is likely representative of the original primary composition.

496

497   **5.4.2.2. Iron isotopes and sedimentary environment**

498   Recently, iron isotopes were proposed as a redox indicator of ancient oceans, resulting from

499   the enrichment of heavy iron isotopes in Fe(III) minerals during the chemical oxidation of dissolved

500   Fe (II) to Fe (III) precipitates (Rouxel et al., 2005; Anbar and Rouxel, 2007). The enrichment of the

501   heavy iron isotopes in the poorly mobile Fe (III)-rich minerals results in the transfer of the light

502   isotopes to the highly mobile Fe (II) phase dissolved in anoxic waters (Dauphas and Rouxel, 2006).

503   The seven whole rock δ^{56}Fe data from the Ibr 1 and Ibr 2 horizons (**Figure 2d**) are divided into

504   ~0.45 ‰ for sample set Ibr 1(n = 3) and ~0.25-0.27 ‰ for Ibr 2 (n = 4).

505   A study showed that the residual iron isotopic composition in magnetite and seawater gradually

506   becomes lighter as the proportion of precipitate increases, implying early magnetite has heavier iron

507   isotopes than late precipitates (Li et al., 2012b). Therefore, the variation of iron isotope composition

508   of the Dujiagou BIFs can be explained by different precipitation stages. However, magnetite as a

509   major BIF mineral, is not an authigenic phase but was probably formed diagenetically from ferro-

510   ferric hydroxide precursors (Ewers, 1983; Klein, 2005; Dauphas et al., 2007a). For example, green

511   rust was considered to be an important magnetite precursor in the Archean ocean (Sumoondur et al.,

512   2008; Zegeye et al., 2012; Sun et al., 2022). Conversion to magnetite with inherited primary δ^{56}Fe

513   values of precursor ferric oxide/hydroxide minerals, probably occur through interaction with

514   hydrothermal Fe^{2+} in the deep marine environments of BIF deposition (Johnson et al., 2008). Hence,

515   the iron isotopes in the BIF indicate changes in the ocean iron cycle as well as changes in

atmospheric redox, preserving a chemical record of Earth's most primitive oceans (Rouxel et al.,
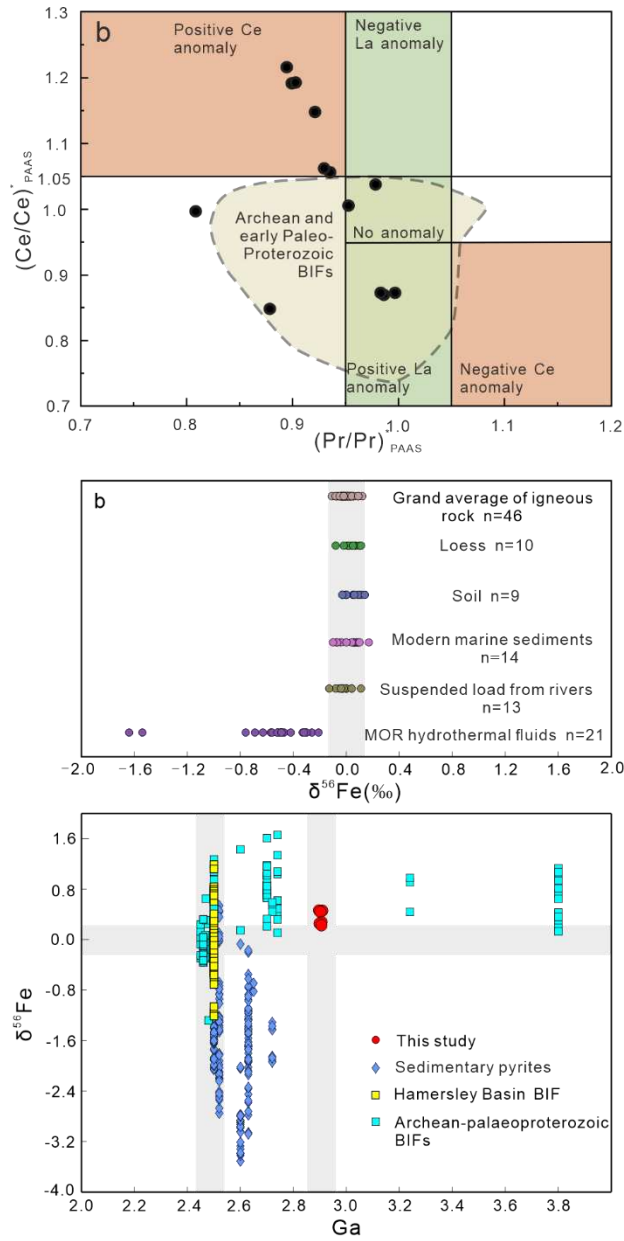
517 2005; Planavsky et al., 2012).

518

519

Figure 8. (a) Ce/Ce* vs. (Pr/Pr*) plot according to Bau and Dulski (1996), (b) Scatter plot of Fe isotopic

composition of igneous rocks, clastic sedimentary rocks and chemically precipitated sedimentary rocks through

Earth history. Igneous rock data from Beard et al. (2003b), other data from (Beard et al., 2003a), (c) whole-

rock δ^{56}Fe values for iron formations from this study and literature (Dauphas et al., 2007b; Johnson et al.,

524   2008; Steinhoefel et al., 2009; Li et al., 2012b; Planavsky et al., 2012; Ye et al., 2017), and δ^{56}Fe values

525   for sedimentary pyrites from Rouxel et al. (2005) and references therein.

526

527   The heavy iron isotope compositions show the opposite behavior expected for modern

528   weathered products and hydrothermal fluids (**Figure 8b**). They indicate that the valence state of iron

529   changed from divalent to trivalent state during the deposition of magnetite. Precambrian BIFs

530   generally exhibit a wide range of δ^{56}Fe values, spanning -1.6 to +1.5 ‰ (**Figure 8c**), with the >0

531   values consistent with partial oxidation of iron, while the <0 values are closer to those produced by

532   dissimilatory Fe(III) reduction, DIR (Lovley et al., 2004). DIR can generate large iron isotope

533   fractionation by reducing trivalent Fe(III) to highly soluble divalent Fe(II) (Beard et al., 1999;

534   Crosby et al., 2007). Previous studies have shown that DIR may have evolved by 3.8 Ga (Craddock

535   and Dauphas, 2011), but the broad absence of negative δ^{56}Fe values in the ＞2.5Ga BIFs, has been

536   taken to indicate that DIR may not have left a strong impact on the Archean iron sedimentary record

537   (Johnson et al., 2008; Czaja et al., 2013). The variable negative δ^{56}Fe values in the Hamersley BIF

538   in Western Australia may thus represent a record of the earliest period of expansive DIR expression

539   in Earth history (**Figure 8c**) (Johnson et al., 2008). Therefore, the consistency of the data with

540   numerous observations for various Archean BIFs, indicate that δ^{56}Fe＞0 is a common characteristic

541   of Archean BIFs, regardless of paleogeographical location (**Figure 8c**). This may be a reflection of

542   the unique nature of biogeochemical cycling of iron during the Archean (Hyslop et al., 2008).

543   Archean black shale pyrites are enriched with light Fe isotopes, with the most negative Fe isotope

544   values being as low as -3.5‰ (**Figure 8c**). Because BIFs are a sink for isotopically heavy iron, black

545   shale pyrite might therefore represent a corresponding reservoir for isotopically light iron in the

546 sedimentary record ([Planavsky et al., 2012](#)). Briefly, divalent Fe(II) is oxidized to trivalent Fe(III),

547 enriching the heavy iron isotopes in the trivalent Fe(III) to form iron oxide-hydroxide. The residual

548 dissolved divalent Fe(II) with its light iron isotopes would have been captured by the pyrite and

549 enriched in pyrite-rich Archean sedimentary rocks. The rich iron oxide content of BIFs indicates the

550 presence of significant Fe(II) oxidants in the Archean upper water column, much of which is debated,

551 considering that the oceans are believed to have been strongly reducing for most of the Archean Eon

552 ([Bekker et al., 2010](#)). The three processes most commonly advocated for iron oxidation in an anoxic

553 atmosphere are; (1) oxidation with O_2 generated by oxygenic photosynthesis, (2) Oxidation by

554 anoxic photosynthesis using Fe (II) as an electron donor rather than H_2O, and (3) Photooxidation

555 ([Dauphas et al., 2007a](#)). Experimental results show that the enrichment of heavy isotopes of iron in

556 Fe(III) minerals occurs during biotic and abiotic oxidation of Fe (II) to Fe(III) under varying redox

557 conditions ([Bullen et al., 2001](#); [Johnson et al., 2002](#); [Welch et al., 2003](#); [Balci et al., 2006](#)), while

558 the possibility of ultraviolet photooxidation in natural seawater compositions may be less likely than

559 previously thought ([Konhauser et al., 2007](#)). The Great Oxidation Event (GOE) led saw the

560 permanent rise of oxygen in the atmosphere, but there is increasing evidence that free oxygen may

561 have predated the GOE ([Brocks et al., 1999](#); [Anbar et al., 2007](#); [Godfrey and Falkowski, 2009](#);

562 [Ostrander et al., 2021](#)). We therefore interpret the prevalence of positive $\delta^{56}Fe$ values in the

563 Dujiagou BIFs as representative of either abiotic and biotic partial oxidation of Fe(II) to Fe(III)

564 minerals, or a combination of both processes. Thus, Archean marine shales and BIFs record iron

565 isotopic composition different from those of modern marine sediments with typical $\delta^{56}Fe$ values of

566 ~0‰ (**Figure 8b**). Collectively, these observations indicate that the Archean oceans were vastly

567 anoxic/hypoxic before the rise of atmospheric oxygen, which as explained above would have

568   influenced the rates and quantitative abiotic and biotic oxidation of mobile Fe(II) in the Archean

569   seawater column to particulate Fe oxide-oxyhydroxides, and therefore exerting a strong control on

570   the $\delta^{56}Fe$ values of particulate and dissolved Fe.

571

572   **6. Conclusions**

573   The Dujiagou BIFs formed in an oceanic setting, probably near a subduction zone, similar to

574   the suggested location where the Algoma-type BIFs that are generally prevalent in the Archean

575   sedimentary rock record, deposited. With a predicted depositional age estimated at >2.90 Ga, the

576   Dujiagou BIFs are likely the oldest BIFs in the Yangtze Craton. Their geochemical composition

577   indicate that they are chemical sediments, marked by a minor detrital component that diluted and

578   masked their primary REE composition.   The data suggest that iron was sourced from submarine

579   hydrothermal fluids, consistent with the origin of iron in most Precambrian BIFs. Moreover, their

580   positive iron isotopic composition is characteristic of primary Archean BIF deposits, indicating that

581   partial oxidation of iron led to the deposition of the divalent magnetite-rich BIFs in an Archean

582   ocean that was broadly reducing.

583

592

References

594   Anbar, A.D., Duan, Y., Lyons, T.W., Arnold, G.L., Kendall, B., Creaser, R.A., Kaufman, A.J., Gordon, G.W., Scott, C., Garvin, J.,
595   Buick, R., 2007. A whiff of oxygen before the Great Oxidation Event? Science, 317(5846): 1903-1906.

596   Anbar, A.D., Rouxel, O., 2007. Metal Stable Isotopes in Paleoceanography. Annual Review of Earth & Planetary Sciences, 35(1):
597   717-746.

598   Atkinson, A., O'Dwyer, M.L., Taylor, R.I., 1983. 55Fe Diffusion in magnetite crystals at 500° and its relevance to the oxidation of
599   fe. Radiation Effects, 75(1-4): 169-172.

600   Balci, N., Bullen, T.D., Witte-Lien, K., Shanks, W.C., Motelica, M., Mandernack, K.W., 2006. Iron isotope fractionation during
601   microbially stimulated Fe(II) oxidation and Fe(III) precipitation. Geochimica et Cosmochimica Acta, 70(3): 622-639.

602   Basta, F.F., Maurice, A.E., Fontboté, L., Favarger, P.Y., 2011. Petrology and geochemistry of the banded iron formation (BIF) of
603   Wadi Karim and Um Anab, Eastern Desert, Egypt: Implications for the origin of Neoproterozoic BIF. Precambrian
604   Research, 187(3-4): 277-292.

605   Bau, M., 1993. Effects of syn- and post-depositional processes on the rare-earth element distribution in Precambrian iron-
606   formations. European Journal of Mineralogy, 5(2): 257-267.

607   Bau, M., Dulski, P., 1996. Distribution of yttrium and rare-earth elements in the Penge and Kuruman iron-formations, Transvaal
608   Supergroup, South Africa. Precambrian Research, 79(1-2): 0-55.

609   Bau, M., Dulski, P., 1999. Comparing yttrium and rare earths in hydrothermal fluids from the Mid-Atlantic Ridge: implications for
610   Y and REE behaviour during near-vent mixing and for the Y/Ho ratio of Proterozoic seawater. Chemical Geology,
611   155(1): 77-90.

612   Beard, B.L., Johnson, C.M., Cox, L., 1999. Iron Isotope Biosignatures. Science, 285(5435): 1889-1892.

613   Beard, B.L., Johnson, C.M., Damm, K.V., Poulson, R.L., 2003a. Iron isotope constraints on Fe cycling and mass balance in
614   oxygenated Earth oceans. Geology, 31(7): 629-632.

615   Beard, B.L., Johnson, C.M., Skulan, J.L., Nealson, K.H., Cox, L., Sun, H., 2003b. Application of Fe isotopes to tracing the
616   geochemical and biological cycling of Fe. Chemical Geology, 195(1): 87-117.

617   Bekker, A., Slack, J.F., Planavsky, N., Krapez, B., Hofmann, A., Konhauser, K.O., Rouxel, O.J., 2010. Iron Formation: The
618   Sedimentary Product of a Complex Interplay among Mantle, Tectonic, Oceanic, and Biospheric Processes. Economic
619   Geology, 105(3): 467-508.

620   Blundy, J., Wood, B., 1994. Prediction of crystal-melt partition coefficients from elastic moduli. Nature, 372(6505): 452-454.

621   Bolhar, R., Kamber, B.S., Moorbath, S., Fedo, C.M., Whitehouse, M.J., 2004. Characterisation of early Archaean chemical
622   sediments by trace element signatures. Earth and Planetary Science Letters, 222(1): 43-60.

623   Bolhar, R., Vankranendonk, M., 2007. A non-marine depositional setting for the northern Fortescue Group, Pilbara Craton, inferred
624   from trace element geochemistry of stromatolitic carbonates. Precambrian Research, 155(3-4): 229-250.

625   Brando Soares, M., Corrêa Neto, A.V., Zeh, A., Cabral, A.R., Pereira, L.F., Prado, M.G.B.d., Almeida, A.M.d., Manduca, L.G.,
626   Silva, P.H.M.d., Mabub, R.O.d.A., Schlichta, T.M., 2017. Geology of the Pitangui greenstone belt, Minas Gerais, Brazil:
627   Stratigraphy, geochronology and BIF geochemistry. Precambrian Research, 291: 17-41.

628   Brocks, J., Logan, G., Buick, R., Summons, R., 1999. Archean molecular fossils and the early rise of eukaryotes. Science 285:
629   1033-1036.

630   Bullen, T.D., White, A.F., Childs, C.W., Vivit, D.V., Schulz, M.S., 2001. Demonstration of significant abiotic iron isotope
631   fractionation in nature. Geology, 29(8): 699-702.

632   Cawood, P.A., Zhao, G., Yao, J., Wang, W., Xu, Y., Wang, Y., 2018. Reconstructing South China in Phanerozoic and Precambrian
633   supercontinents. Earth-Science Reviews, 186: 173-194.

634   Charvet, J., 2013. The Neoproterozoic–Early Paleozoic tectonic evolution of the South China Block: An overview. Journal of Asian
635   Earth Sciences, 74: 198-209.

636   Chen, K., Gao, S., Wu, Y., Guo, J., Hu, Z., Liu, Y., Zong, K., Liang, Z., Geng, X., 2013. 2.6–2.7Ga crustal growth in Yangtze craton,
637   South China. Precambrian Research, 224: 472-490.

638   Chi Fru, E., Ivarsson, M., Kilias, S.P., Bengtson, S., Belivanova, V., Marone, F., Fortin, D., Broman, C., Stampanoni, M., 2013.
639   Fossilized iron bacteria reveal a pathway to the biological origin of banded iron formation. Nature Communications, 4:
640   2050.

641   Chi Fru, E., Kilias, S., Ivarsson, M., Rattray, J., Gkika, K., McDonald, I., He, Q., Broman, C., 2018. Sedimentary mechanisms of
642   a modern banded iron formation on Milos Island, Greece-Supplement. Solid Earth, 9: 573-598.

643   Chi Fru, E., Rodriguez, N.P., Partin, C.A., Lalonde, S.V., Andersson, P., Weiss, D.J., El Albani, A., Rodushkin, I., Konhauser, K.O.,
644   2016. Cu isotopes in marine black shales record the Great Oxidation Event. Proceedings of the National Academy of
645   Sciences of the United States of America, 113(18): 4941-4946.

646   Craddock, P.R., Dauphas, N., 2011. Iron and carbon isotope evidence for microbial iron respiration throughout the Archean. Earth
647   and Planetary Science Letters, 303(1): 121-132.

648   Crosby, H.A., Roden, E.E., Johnson, C.M., Beard, B.L., 2007. The mechanisms of iron isotope fractionation produced during
649   dissimilatory Fe(III) reduction by Shewanella putrefaciens and Geobacter sulfurreducens. Geobiology, 5(2): 169-189.

650   Crowley, J.L., Myers, J.S., Dunning, G.R., 2002. Timing and nature of multiple 3700-3600 Ma tectonic events in intrusive rocks
651   north of the Isua greenstone belt, southern West Greenland. Geological Society of America Bulletin, 114(10): 1311-
652   1325.

653   Cui, M.L., Zhang, L.C., Wu, H.Y., Xu, Y.X., Li, W.J., 2014. Timing and tectonic setting of the Sijiaying banded iron deposit in the
654   eastern Hebei province, North China Craton: Constraints from geochemistry and SIMS zircon U-Pb dating. Journal of
655   Asian Earth Sciences, 94: 240-251.

656   Czaja, A.D., Johnson, C.M., Beard, B.L., Roden, E.E., Li, W., Moorbath, S., 2013. Biological Fe oxidation controlled deposition
657   of banded iron formation in the ca. 3770Ma Isua Supracrustal Belt (West Greenland). Earth and Planetary Science
658   Letters, 363: 192-203.

659   Dauphas, N., Cates, N.L., Mojzsis, S.J., Busigny, V., 2007a. Identification of chemical sedimentary protoliths using iron isotopes
660   in the >3750 Ma Nuvvuagittuq supracrustal belt, Canada. Earth and Planetary Science Letters, 254(3-4): 358-376.

661   Dauphas, N., Rouxel, O., 2006. Mass spectrometry and natural variations of iron isotopes. Mass Spectrometry Reviews, 25(4):
662   515-550.

663   Dauphas, N., van Zuilen, M., Wadhwa, M., Davis, A.M., Marty, B., Janney, P.E., 2004. Clues from Fe isotope variations on the
664   origin of early Archean BIFs from Greenland. Science, 306(5704): 2077-2080.

665   Dauphas, N., Zuilen, M.V., Busigny, V., Lepland, A., Wadhwa, M., Janney, P.E., 2007b. Iron isotope, major and trace element
666   characterization of early Archean supracrustal rocks from SW Greenland: Protolith identification and metamorphic
667   overprint. Geochimica et Cosmochimica Acta, 71(19): 4745-4770.

668   Ewers, W.E., 1983. Chapter 13 Chemical Factors in the Deposition and Diagenesis of Banded Iron-Formation. Iron Formations:
669   Facts and Problems, 6: 491-512.

670   Farquhar, J., Bao, H.M., Thiemens, M., 2000. Atmospheric influence of Earth's earliest sulfur cycle. Science, 289(5480): 756-758.

671   Finger, F., Broska, I., Roberts, M.P., Schermaier, A., 1998. Replacement of primary monazite by apatite-allanite-epidote coronas
672   in an amphibolite facies granite gneiss from the eastern Alps. AMERICAN MINERALOGIST, 83(3-4): 248-258.

673   Frost, C.D., von Blanckenburg, F., Schoenberg, R., Frost, B.R., Swapp, S.M., 2006. Preservation of Fe isotope heterogeneities
674   during diagenesis and metamorphism of banded iron formation. Contributions to Mineralogy and Petrology, 153(2):
675   211.

676 Gao, S., Ling, W., Qiu, Y., Lian, Z., Hartmann, G., Simon, K., 1999. Contrasting geochemical and Sm-Nd isotopic compositions
677   of Archean metasediments from the Kongling high-grade terrain of the Yangtze craton: Evidence for cratonic evolution
678   and redistribution of REE during crustal anatexis. 63: 2071-2088.

679 Gao, S., Yang, J., Zhou, L., Li, M., Hu, Z., Guo, J., Yuan, H., Gong, H., Xiao, G., Wei, J., 2011. Age and growth of the Archean
680   Kongling terrain, South China, with emphasis on 3.3 ga granitoid gneisses. 311(2): 153-182.

681 Gao, S., Zhang, B.R., 1990. The discovery of Archean TTG gneisses in northern Yangtze craton and their implications. Earth
682   Science, 15: 675-679.

683 Ghosh, R., Baidya, T.K., 2017. Mesoarchean BIF and iron ores of the Badampahar greenstone belt, Iron Ore Group, East Indian
684   Shield. Journal of Asian Earth Sciences, 150: 25-44.

685 Godfrey, L.V., Falkowski, P.G., 2009. The cycling and redox state of nitrogen in the Archaean ocean. Nature Geoscience, 2(10):
686   725-729.

687 Goodwin, A., 1973. Archean Iron-Formations and Tectonic basins of the Canadian Shield. Economic Geology, 68: 915-933.

688 Guo, J.-L., Wu, Y.-B., Gao, S., Jin, Z.-M., Zong, K.-Q., Hu, Z.-C., Chen, K., Chen, H.-H., Liu, Y.-S., 2015. Episodic Paleoarchean-
689   Paleoproterozoic (3.3–2.0Ga) granitoid magmatism in Yangtze Craton, South China: Implications for late Archean
690   tectonics. Precambrian Research, 270: 246-266.

691 Guo, Q.J., Strauss, H., Kaufman, A.J., Schroder, S., Gutzmer, J., Wing, B., Baker, M.A., Bekker, A., Jin, Q.S., Kim, S.T., Farquhar,
692   J., 2009. Reconstructing Earth's surface oxidation across the Archean-Proterozoic transition. Geology, 37(5): 399-402.

693 Hagemann, S.G., Angerer, T., Duuring, P., Rosière, C.A., Figueiredo e Silva, R.C., Lobato, L., Hensler, A.S., Walde, D.H.G., 2016.
694   BIF-hosted iron mineral system: A review. Ore Geology Reviews, 76: 317-359.

695 Han, Q.S., Peng, S.B., Kusky, T., Polat, A., Jiang, X.F., Cen, Y., Liu, S.F., Deng, H., 2017. A Paleoproterozoic ophiolitic melange,
696   Yangtze craton, South China: Evidence for Paleoproterozoic suturing and microcontinent amalgamation. Precambrian
697   Research, 293: 13-38.

698 Han, Q.S., Peng, S.B., Polat, A., Kusky, T., Deng, H., Wu, T.Y., 2018. A ca.2.1 Ga Andean-type margin built on metasomatized
699   lithosphere in the northern Yangtze craton, China: Evidence from high-Mg basalts and andesites. Precambrian Research,
700   309: 309-324.

701 Haug Aa Rd, R., Frei, R., Stendal, H., Konhauser, K., 2013. Petrology and geochemistry of the 2.9 Ga Itilliarsuk banded iron
702   formation and associated supracrustal rocks, West Greenland: Source characteristics and depositional environment.
703   Precambrian Research, 229: 150-176.

704 He, Y.S., Ke, S., Teng, F.Z., Wang, T.T., Wu, H.J., Lu, Y.H., Li, S.G., 2015. High-Precision Iron Isotope Analysis of Geological
705   Reference Materials by High-Resolution MC-ICP-MS. Geostandards and Geoanalytical Research, 39(3): 341-356.

706 Hoffman, P.F., Kaufman, A.J., Halverson, G.P., Schrag, D.P., 1998. A Neoproterozoic snowball earth. Science, 281(5381): 1342-
707   1346.

708 Holland, H.D., 2006. The oxygenation of the atmosphere and oceans. Philosophical Transactions of the Royal Society B-Biological
709   Sciences, 361(1470): 903-915.

710 Hoskin, P.W.O., Black, L.P., 2000. Metamorphic zircon formation by solid-state recrystallization of protolith igneous zircon.
711   Journal of Metamorphic Geology, 18(4): 423-439.

712 Hu, Z., Zhang, W., Liu, Y., Gao, S., Li, M., Zong, K., Chen, H., Hu, S., 2015. "Wave" Signal-Smoothing and Mercury-Removing
713   Device for Laser Ablation Quadrupole and Multiple Collector ICPMS Analysis: Application to Lead Isotope Analysis.
714   Analytical Chemistry, 87(2): 1152-1157.

715 Huang, B., Kusky, T.M., Wang, L., Deng, H., Wang, J.P., Fu, D., Peng, H.T., Ning, W.B., 2019. Age and genesis of the Neoarchean
716   Algoma-type banded iron formations from the Dengfeng greenstone belt, southern North China Craton:
717   Geochronological, geochemical and Sm-Nd isotopic constraints. Precambrian Research, 333.

718 Huang, H., Fryer, B.J., Polat, A., Pan, Y., 2014. Amphibole, plagioclase and clinopyroxene geochemistry of the Archean
719   Fiskenæsset Complex at Majorqap qâva, southwestern Greenland: Implications for Archean petrogenetic and

720   geodynamic processes. Precambrian Research, 247: 64-91.

721   Hyslop, E.V., Valley, J.W., Johnson, C.M., Beard, B.L., 2008. The effects of metamorphism on O and Fe isotope compositions in

722   the Biwabik Iron Formation, northern Minnesota. Contributions to Mineralogy & Petrology, 155(3): 313-328.

723   Jackson, S.E., Pearson, N.J., Griffin, W.L., Belousova, E.A., 2004. The application of laser ablation-inductively coupled plasma-

724   mass spectrometry to in situ U–Pb zircon geochronology. Chemical Geology, 211(1): 47-69.

725   Jenner, F.E., Bennett, V.C., Nutman, A.P., Friend, C.R.L., Norman, M.D., Yaxley, G., 2009. Evidence for subduction at 3.8 Ga:

726   Geochemistry of arc-like metabasalts from the southern edge of the Isua Supracrustal Belt. Chemical Geology, 261(1-

727   2): 82-97.

728   Ji, W.B., Lin, W., Faure, M., Chu, Y., Wu, L., Wang, F., Wang, J., Wang, Q.C., 2014. Origin and tectonic significance of the

729   Huangling massif within the Yangtze craton, South China. Journal of Asian Earth Sciences, 86: 59-75.

730   Jiang, J., 1986. Isotopic geochronology and crustal evolution of the Huangling metamorphic terrain. Journal of Jiling University

731   (Earth Science Edition), 3: 1-11.

732   Jiang, X.F., Peng, S.B., Polat, A., Kusky, T., Wang, L., Wu, T.Y., Lin, M.S., Han, Q.S., 2016. Geochemistry and geochronology of

733   mylonitic metasedimentary rocks associated with the Proterozoic Miaowan Ophiolite Complex, Yangtze craton, China:

734   Implications for geodynamic events. Precambrian Research, 279: 37-56.

735   Johnson, C.M., Beard, B.L., Beukes, N.J., Klein, C., O'Leary, J.M., 2003. Ancient geochemical cycling in the Earth as inferred

736   from Fe isotope studies of banded iron formations from the Transvaal Craton. Contributions to Mineralogy and

737   Petrology, 144(5): 523-547.

738   Johnson, C.M., Beard, B.L., Klein, C., Beukes, N.J., Roden, E.E., 2008. Iron isotopes constrain biologic and abiologic processes

739   in banded iron formation genesis. Geochimica Et Cosmochimica Acta, 72(1): 151-169.

740   Johnson, C.M., Skulan, J.L., Beard, B.L., Sun, H., Nealson, K.H., Braterman, P.S., 2002. Isotopic fractionation between Fe(III)

741   and Fe(II) in aqueous solutions. Earth and Planetary Science Letters, 195(1-2): 141-153.

742   Kang, C., Shan, G., Wu, Y., Guo, J., Hu, Z., Liu, Y., Zong, K., Liang, Z., Geng, X., 2013. 2.6–2.7 Ga crustal growth in Yangtze

743   craton, South China. Precambrian Research, 224(none): 472-490.

744   Kasting, J.F., 2013. What caused the rise of atmospheric O 2 ? Chemical Geology, 362(362): 13-25.

745   Klein, C., 2005. Some Precambrian banded iron-formations (BIFs) from around the world: Their age, geologic setting, mineralogy,

746   metamorphism, geochemistry, and origins. American Mineralogist, 90(10): 1473-1499.

747   Konhauser, K.O., Amskold, L., Lalonde, S.V., Posth, N.R., Kappler, A., Anbar, A.D., 2007. Decoupling photochemical Fe(II)

748   oxidation from shallow-water BIF deposition. Earth and Planetary Science Letters, 258(1-2): 87-100.

749   Li, H.M., Zhang, Z.J., Li, L.X., Zhang, Z.C., Chen, J., Yao, T., 2014a. Types and general characteristics of the BIF-related iron

750   deposits in China. Ore Geology Reviews, 57: 264-287.

751   Li, L.M., Lin, S.F., Davis, D.W., Xiao, W.J., Xing, G.F., Yin, C.Q., 2014b. Geochronology and geochemistry of igneous rocks from

752   the Kongling terrane: Implications for Mesoarchean to Paleoproterozoic crustal evolution of the Yangtze Block.

753   Precambrian Research, 255: 30-47.

754   Li, W., Beard, B.L., Johnson, C.M., 2015. Biologically recycled continental iron is a major component in banded iron formations.

755   112: 8193-8198.

756   Li, X.H., Li, Z.X., Ge, W., Zhou, H., Li, W., Liu, Y., Wingate, M.T., 2003. Neoproterozoic granitoids in South China: crustal melting

757   above a mantle plume at ca. 825 Ma? Precambrian Research, 122: 45-83.

758   Li, Y.H., Hou, K.J., Wan, D.F., Zhang, Z.J., 2012a. A compare geochemistry study for Algoma- and Superior-type banded iron

759   formations. Acta Petrologica Sinica, 28(11): 3513-3519.

760   Li, Z.H., Zhu, X.K., Tang, S.H., 2012b. Fe isotope compositions of banded iron formation from Anshan-Benxi area: Constraints

761   on the formation mechanism and Archean ocean environment. Acta Petrologica Sinica, 28(11): 3545-3558.

762   Ling, W.L., Gao, S., Zhang, B.R., Zhou, L., Xu, D.L., 2001. The recognizing of ca. 1.95 Ga tectono-thermal eventin Kongling

763   nucleus and its significance for the evolution of Yangtze Block, South China. Chinese Science Bulletin, 46: 326-329.

764 Lovley, D.R., Holmes, D.E., Nevin, K.P., 2004. Dissimilatory Fe(III) and Mn(IV) reduction. In: Poole, R.K. (Ed.), Advances in
765   Microbial Physiology, Vol. 49. Advances in Microbial Physiology, pp. 219-286.

766 Ludwig, K., 2000. Users manual for Isoplot/Ex: a geochronological toolkit for Microsoft Excel. Berkeley Geochronology Center
767   Spec. Publ., 1a: 53.

768 Lyons, T.W., Reinhard, C.T., Planavsky, N.J., 2014. The rise of oxygen in Earth's early ocean and atmosphere. Nature, 506(7488):
769   307-315.

770 Ma, D.Q., Du, S.H., Xiao, Z.F., 2002. The origin of Huangling granite batholith. Acta Petrol. Mineral., 21: 151-161.

771 Mloszewska, A.M., Pecoits, E., Cates, N.L., Mojzsis, S.J., O'Neil, J., Robbins, L.J., Konhauser, K.O., 2012. The composition of
772   Earth's oldest iron formations: The Nuvvuagittuq Supracrustal Belt (Quebec, Canada). Earth and Planetary Science
773   Letters, 317: 331-342.

774 Morris, R.C., 1993. Genetic modelling for banded iron-formation of the Hamersley Group, Pilbara Craton, Western Australia.
775   Precambrian Research, 60(1): 243-286.

776 Myers, J.S., 2001. Protoliths of the 3.8–3.7 Ga Isua greenstone belt, West Greenland. Precambrian Research, 105(2): 129-141.

777 Ndime, E.N., Ganno, S., Nzenti, J.P., 2019. Geochemistry and Pb-Pb geochronology of the Neoarchean Nkout West
778   metamorphosed banded iron formation, southern Cameroon. International Journal of Earth Sciences, 108(5): 1551-1570.

779 Nozaki, Y., Zhang, J., Amakawa, H., 1997. The fractionation between Y and Ho in the marine environment. Earth and Planetary
780   Science Letters, 148(1-2): 329-340.

781 Och, L.M., Shields-Zhou, G.A., 2012. The Neoproterozoic oxygenation event: Environmental perturbations and biogeochemical
782   cycling. Earth-Science Reviews, 110(1): 26-57.

783 Ostrander, C., Johnson, A., Anbar, A., 2021. Earth's First Redox Revolution. Annual Review of Earth and Planetary Sciences, 49:
784   337-366.

785 Pecoits, E., Gingras, M.K., Barley, M.E., Kappler, A., Posth, N.R., Konhauser, K.O., 2009. Petrography and geochemistry of the
786   Dales Gorge banded iron formation: Paragenetic sequence, source and implications for palaeo-ocean chemistry.
787   Precambrian Research, 172(1): 163-187.

788 Peng, M., Wu, Y., Gao, S., Zhang, H., Wang, J., Liu, X., Gong, H., Zhou, L., Hu, Z., Liu, Y., Yuan, H., 2012a. Geochemistry, zircon
789   U–Pb age and Hf isotope compositions of Paleoproterozoic aluminous A-type granites from the Kongling terrain,
790   Yangtze Block: Constraints on petrogenesis and geologic implications. Gondwana Research, 22(1): 140-151.

791 Peng, M., Wu, Y.B., Wang, J., Jiao, W.F., Liu, X.C., Yang, S.H., 2009. Paleoproterozoic mafic dyke from Kongling terrain in the
792   Yangtze Craton and its implication. Chinese Science Bulletin, 54(6): 1098-1104.

793 Peng, S.B., Kusky, T.M., Jiang, X.F., Wang, L., Wang, J.P., Deng, H., 2012b. Geology, geochemistry, and geochronology of the
794   Miaowan ophiolite, Yangtze craton: Implications for South China's amalgamation history with the Rodinian
795   supercontinent. Gondwana Research, 21(2-3): 577-594.

796 Planavsky, N., Rouxel, O.J., Bekker, A., Hofmann, A., Little, C., Lyons, T.W., 2012. Iron isotope composition of some Archean
797   and Proterozoic iron formations. Geochimica Et Cosmochimica Acta, 80(none): 158-169.

798 Polat, A., Frei, R., 2005. The origin of early Archean banded iron formations and of continental crust, Isua, southern West Greenland.
799   Precambrian Research, 138(1-2): 151-175.

800 Poulton, S.W., Canfield, D.E., 2011. Ferruginous Conditions: A Dominant Feature of the Ocean through Earth's History. Elements,
801   7(2): 107-112.

802 Qiu, X.-F., Ling, W.-L., Liu, X.-M., Lu, S.-S., Jiang, T., Wei, Y.-X., Peng, L.-H., Tan, J.-J., 2018. Evolution of the Archean
803   continental crust in the nucleus of the Yangtze block: Evidence from geochemistry of 3.0 Ga TTG gneisses in the
804   Kongling high-grade metamorphic terrane, South China. Journal of Asian Earth Sciences, 154: 149-161.

805 Qiu, Y.M., Gao, S., McNaughton, N.J., Groves, D.I., Ling, W., 2000. First evidence of > 3.2 Ga continental crust in the Yangtze
806   craton of south China and its implications for Archean crustal evolution and Phanerozoic tectonics. Geology, 28(1): 11-
807   14.

808 Rouxel, O.J., Bekker, A., Edwards, K.J., 2005. Iron isotope constraints on the Archean and Paleoproterozoic ocean redox state.
809   Science, 307(5712): 1088-1091.

810 Rubatto, D., 2017. Zircon: The Metamorphic Mineral. Reviews in Mineralogy & Geochemistry, 83(1): 261-296.

811 Singh, V.K., Slabunov, A., 2015. The Central Bundelkhand Archaean greenstone complex, Bundelkhand craton, central India:
812   geology, composition, and geochronology of supracrustal rocks. International Geology Review, 57(11-12): 1349-1364.

813 Smith, A.B., 2018. The Iron Formations of Southern Africa. Geology of Southwest Gondwana.

814 Steinhoefel, G., Horn, I., Blanckenburg, F.V., 2009. Micro-scale tracing of Fe and Si isotope signatures in banded iron formation
815   using femtosecond laser ablation. Geochimica Et Cosmochimica Acta, 73(18): 5343-5360.

816 Sumoondur, A., Shaw, S., Ahmed, I., Benning, L.G., 2008. Green rust as a precursor for magnetite: an in situ synchrotron based
817   study. Mineralogical Magazine, 72(1): 201-204.

818 Sun, McDonough, 1989. Chemical and isotopic systematics of oceanic basalts: Implications for mantle composition and processes.
819   Geological Society London Special Publications, 42(1).

820 Sun, L., Lechte, M., Shi, X., Zhou, X., Zhou, L., Fang, H., Xie, B., Wu, M., Tang, D., 2022. Hexagonal magnetite in Algoma-type
821   banded iron formations of the ca. 2.52 Ga Baizhiyan Formation, North China: Evidence for a green rust precursor?
822   American Mineralogist, 107(5): 970-984.

823 Viehmann, S., Hoffmann, J.E., Münker, C., Bau, M., 2014. Decoupled Hf-Nd isotopes in Neoarchean seawater reveal weathering
824   of emerged continents. Geology, 42(2): 115-118.

825 Wang, C., Wu, H., Li, W., Peng, Z., Zhang, L., Zhai, M., 2017. Changes of Ge/Si, REE+Y and SmNd isotopes in alternating Fe-
826   and Si-rich mesobands reveal source heterogeneity of the ~2.54Ga Sijiaying banded iron formation in Eastern Hebei,
827   China. Ore Geology Reviews, 80: 363-376.

828 Wang, C.L., Zhang, L.C., Lan, C.Y., Dai, Y.P., 2014. Rare earth element and yttrium compositions of the Paleoproterozoic
829   Yuanjiacun BIF in the Lüliang area and their implications for the Great Oxidation Event (GOE). Science China: Earth
830   Sciences, 57: 2469-2485.

831 Warchola, T., Lalonde, S.V., Pecoits, E., von Gunten, K., Robbins, L.J., Alessi, D.S., Philippot, P., Konhauser, K.O., 2018. Petrology
832   and geochemistry of the Boolgeeda Iron Formation, Hamersley Basin, Western Australia. Precambrian Research, 316:
833   155-173.

834 Wei, J., 2021. Petrology and geochemistry of the Archean Huangling greenstone belt in the Yangtze Craton, South China.
835   Precambrian Research, 364: 106340.

836 Wei, J., Wei, Y., Wang, J., Wang, X., 2020. Geochronological constraints on the formation and evolution of the Huangling basement
837   in the Yangtze craton, South China. Precambrian Research, 342: 105707.

838 Wei, J.Q., Jing, M.M., 2013. Chronology and geochemistry of amphibolites from the Kongling complex. Chinese Journal of Gology,
839   48(4): 970-983.

840 Wei, J.Q., Wang, J.X., 2012. Zircon age and Hf isotope compositions of amphibolite enclaves from the Kongling complex.
841   Geological Journal of China Universities, 18(4): 589-600.

842 Wei, Y.X., Zhou, W.X., Hu, Z.X., Li, H.Q., Huang, X.X., Zhao, X.M., Xu, D.L., 2019. Geochronology and Geochemistry of
843   Archean TTG and Tremolite Schist Xenoliths in Yemadong Complex: Evidence for >= 3.0 Ga Archean Continental
844   Crust in Kongling High-Grade Metamorphic Terrane, Yangtze Craton, China. Minerals, 9(11).

845 Welch, S.A., Beard, B.L., Johnson, C.M., Braterman, P.S., 2003. Kinetic and equilibrium Fe isotope fractionation between aqueous
846   Fe(II) and Fe(III). Geochimica Et Cosmochimica Acta, 67(22): 4231-4250.

847 Wu, C., Yang, T., Shields, G.A., Bian, X., Gao, B., Ye, H., Li, W., 2020. Termination of Cryogenian ironstone deposition by deep
848   ocean euxinia. Geochemical Perspectives Letters, 15: 1-5.

849 Xiong, C.Y., Wei, C.S., Jin, G.F., Tan, W.Q., Li, W.X., 2004. Pre-sinian paleostructural framework and major geological events in
850   the huangling anticline, western hubei. Journal of Geomechanics, 10(2): 97-112.

851 Yakymchuk, C., Kirkland, C.L., Clark, C., 2018. Th/U ratios in metamorphic zircon. Journal of Metamorphic Geology, 36(6): 715-

737.

Yang, X., Mao, J., Santosh, M., Li, R., Wu, C., Gao, J., Zhang, X., Wang, Z., 2022. Ediacaran iron formations from the North Qilian Orogenic Belt, China: Age, geochemistry, Sm–Nd isotopes and link with submarine volcanism. Precambrian Research, 368: 106498.

Ye, H., Wu, C.Z., Yang, T., Santosh, M., Yao, X.Z., Gao, B.F., Wang, X.L., Li, W.Q., 2017. Updating the Geologic Barcodes for South China: Discovery of Late Archean Banded Iron Formations in the Yangtze Craton. Scientific Reports, 7.

Zegeye, A., Bonneville, S.C., Benning, L., Sturm, A., Fowle, D., Jones, C., Canfield, D., Ruby, C., Maclean, L., Nomosatryo, S., Crowe, S., Poulton, S., 2012. Green rust formation controls nutrient availability in a ferruginous water column. Geology, 40(7): 599-602.

Zhai, M.G., 2013. The main old lands in China and assembly of Chinese unified continent. Science China Earth Sciences, 56(11): 1829-1852.

Zhang, L.C., Zhai, M.G., Wan, Y.S., Guo, J.H., Dai, Y.P., Wang, C.L., Liu, L., 2012. Study of the Precambrian BIF-iron deposits in the North China Craton: Progresses and questions. Acta Petrologica Sinica, 28(11): 3431-3445.

Zhang, S.-B., Zheng, Y.-F., Wu, Y.-B., Zhao, Z.-F., Gao, S., Wu, F.-Y., 2006. Zircon isotope evidence for ≥3.5Ga continental crust in the Yangtze craton of China. Precambrian Research, 146(1): 16-34.

Zhang, S.B., Zheng, Y.F., 2013. Formation and evolution of Precambrian continental lithosphere in South China. Gondwana Research, 23(4): 1241-1260.

Zhao, G., Guo, J., 2012. Precambrian geology of China: Preface. Precambrian Research, 222-223: 1-12.

Zhao, G.C., Cawood, P.A., 2012. Precambrian geology of China. Precambrian Research, 222: 13-54.

Zhao, J.-H., Zhou, M.-F., Zheng, J.-P., 2013. Neoproterozoic high-K granites produced by melting of newly formed mafic crust in the Huangling region, South China. Precambrian Research, 233: 93-107.

Zhao, J.H., Zhou, M.F., 2007. Geochemistry of Neoproterozoic mafic intrusions in the Panzhihua district (Sichuan Province, SW China): Implications for subduction-related metasomatism in the upper mantle. Precambrian Research, 152(1-2): 27-47.

Zheng, J., Griffin, W.L., O'Reilly, S.Y., Zhang, M., Pearson, N., Pan, Y.J.G., 2006. Widespread Archean basement beneath the Yangtze craton. 34: 417.

Zhou, Z., Wei, X.Y., Mou, Z.Y., Li, F.H., D, Q.F., 2019. New Progresses in Geological Survey of Huangling Basement, Yangtze Craton. Resources Environment＆Engineering, 33(S1): 1-6.

Zong, K.Q., Klemd, R., Yuan, Y., He, Z.Y., Guo, J.L., Shi, X.L., Liu, Y.S., Hu, Z.C., Zhang, Z.M., 2017. The assembly of Rodinia: The correlation of early Neoproterozoic (ca. 900 Ma) high-grade metamorphism and continental arc formation in the southern Beishan Orogen, southern Central Asian Orogenic Belt (CAOB). Precambrian Research, 290: 32-48.